NTNU – Trondheim
Norwegian University of
Science and Technology

Permeation and Mechanical Properties of Porous Supports Intended for Asymmetric Membranes Based on La(0.2)Sr(0.8)Fe(0.8)Al(0.2)O(3-δ)

Dan Stræte Lagergren

Chemical Engineering and Biotechnology
Submission date: December 2012
Supervisor: Kjell Wiik, IMTE
Co-supervisor: Ørjan Fossmark Lohne, IMT
Jonas Gurauskis, IMT

Norwegian University of Science and Technology
Department of Materials Science and Engineering

Declaration

I hereby declare that the work presented in this Master Thesis has been performed independently and in accordance with the rules and regulations for examination at the Norwegian University of Science and Technology (NTNU).

Dan Stræte Lagergren

December 15, 2012

Preface

This Master thesis is submitted to the Department of Materials Science and Engineering at the Norwegian University of Science and Technology as a part of the requirements to obtain the degree Master of Science (Sivilingeniør). The work presented in this thesis was done between 22 July and 15 December 2012.

The work was done under the guidance from the Author's supervisor Prof. Kjell Wiik, and co-supervisors Dr. Jonas Gurauskis, and PhD-student Ørjan Fossmark Lohne. Their combined help has been invaluable. I personally want to thank all of the above for the time and effort they have given to guide me through this thesis work. I feel a deep appreciation and gratitude to them all.

I would also like to thank Professor Tor Grande for helpful insight on general solid state chemistry topics. Also I would like to acknowledge my co-workers in the ceramics group. They have all given constructive feedback on thoughts and ideas on practical problems encountered while working on this thesis. Finally I would like to thank the technical staff at the department, especially Julian Tolchard for many fruitful talks on various topics.

Abstract

Production of asymmetric ceramic membranes intended for oxygen gas separation was done by producing porous supports made from coarse $La_{0.2}Sr_{0.8}Fe_{0.8}Al_{0.2}O_{3\text{-}\delta}$ powder produced by the solid state reaction method. The porous support was made by adding 40 vol% carbon black as a pore former to a slip which was tape casted. The tape casted green body was dip-coated with a solution of nano-sized $La_{0.2}Sr_{0.8}Fe_{0.8}Al_{0.2}O_{3\text{-}\delta}$ particles produced by spray pyrolysis, and fired. The asymmetric membranes produced during this work was not gas tight, and thus not viable to use for oxygen gas separation.

Phase pure $La_{0.2}Sr_{0.8}Fe_{0.8}Al_{0.2}O_{3\text{-}\delta}$ was not prepared by the solid state reaction method in this work, and possible reasons for this is discussed.

The gas permeability of the porous support was measured at room temperature. The gas permeability at elevated temperatures was calculated for different pressure drops across the porous support and the estimated gas permeability at elevated temperatures seems promising (58 $\mathrm{mL{\cdot}min^{-1}{\cdot}cm^{-2}}$ at 1000°C, $\Delta p = 10\mathrm{mbar}$). The porosity of the porous support was determined to 62.3 % by Archimedes method, this seems plausible when comparing the results with SEM micrographs.

Due to time restraints during this work no mechanical testing of the porous supports was done.

Sammendrag

Produksjon av asymmetriske keramiske membraner tiltenkt for oksygengass separasjon ble gjort ved å legge et tynt tett funksjonelt lag på porøse støtter med sammensetning $La_{0.2}Sr_{0.8}Fe_{0.8}Al_{0.2}O_{3\text{-}\delta}$. De porøse støttene ble laget av et grovt $La_{0.2}Sr_{0.8}Fe_{0.8}Al_{0.2}O_{3\text{-}\delta}$ pulver syntetisert fra faststoffs metoden. Den porøse støtten ble laget ved å tilsette 40 vol% carbon black til en slikker som ble båndstøpt. Den båndstøpte grønnkroppen ble dyppet i en løsning med $La_{0.2}Sr_{0.8}Fe_{0.8}Al_{0.2}O_{3\text{-}\delta}$ nano-partikler, som utgjør det tynne tette funksjonelle laget. Deretter ble grønnkroppen sintret. De asymmetriske membranene produsert i dette arbeidet ble ikke gasstette, og kunne derfor ikke brukes til oksygengass separasjon.

Faserent $La_{0.2}Sr_{0.8}Fe_{0.8}Al_{0.2}O_{3\text{-}\delta}$ ble ikke produsert med faststoff metoden i dette arbeidet, og mulige grunner til det vil bli diskutert.

Gass permeabiliteten til den porøse støtten ble målt ved romtemperatur. Gass permeabiliteten ved høyere temperaturer ble estimert for forskjellige trykkfall på tvers av den porøse støtten, og den estimerte gass permeabiliteten ser lovende ut (58 $\text{mL}\cdot\text{min}^{-1}\cdot\text{cm}^{-2}$ ved 1000°C, $\Delta p = 10\text{mbar}$). Porøsiteten ble bestemt til 62.3 % med Arkimedes metode, og dette virker troverdig når man sammenligner resultatet med SEM bilder.

På grunn av tidsmangel ble det ikke gjort mekanisk testing av de porøse støttene.

Table of Content

Declaration iii

Preface v

Abstract vii

Sammendrag ix

Abbreviations xiii

List of Figures xvi

List of Tables xvii

1 Introduction 1

2 Theory and Literature Review 3
- 2.1 Structure and Stability of Perovskite Type Oxides 3
- 2.2 Oxygen Transport in Dense MIEC Membranes 8
- 2.3 Asymmetric Membranes 12
  - 2.3.1 Gas Flow in Porous Materials 12
  - 2.3.2 Permeability of Porous Materials 14

3 Experimental 17
- 3.1 Chemicals and Apparatus 17
  - 3.1.1 Chemicals 17
  - 3.1.2 Apparatus 18
- 3.2 Procedure 21
  - 3.2.1 LSFAl powder synthesis 21
  - 3.2.2 Production of Porous Support 24
  - 3.2.3 Applying Dense Functional Layer 26
- 3.3 Characterization of Powder and Membrane Properties 28
  - 3.3.1 Phase Determination 28
  - 3.3.2 Particle Size Distribution and Surface Area Determination 28
  - 3.3.3 Linear Shrinkage 28

3.3.4 Density and Porosity Determination 28
3.3.5 Morphology by SEM 29
3.3.6 Porous Support Permeability Measurements 29

4 Results 31
4.1 LSFAl Powder Synthesis 31
4.1.1 Particle Morphology 31
4.1.2 Phase Purity 32
4.1.3 Densification Behaviour 37
4.1.4 Particle Size Distribution 38
4.1.5 Powder Surface Area 39
4.2 Porous Support Production 40
4.2.1 Phase Purity 40
4.2.2 Morphology 41
4.2.3 Porosity 45
4.2.4 Gas Permeability of Porous Support 45
4.3 Asymmetric Membrane Production 48
4.3.1 Phase Purity 48
4.3.2 Morphology 49

5 Discussion 53
5.1 LSFAl Powder Synthesis 53
5.2 Porous Support Production 57
5.3 Asymmetric Membrane Production 60

6 Concluding Remarks and Further Work 63

References 68

Appendix I

A Calculation of the Goldschmidt Tolerance Factor I

B Tables of Batch compositions III

C Calculation of the amount of different precursors needed to make LSFAl VII

D Calculations of True Porosity IX

E Surface Area Weighted Mean XI

F BET Measurement Data XIII

G EDS of Asymmetric Membrane XV

H Topas analysis - amount of the Secondary Phase XVII

Abbreviations

E.g.	Exempli gratia (for example/such as)
EtOH	Ethanol
F.O.	First occurrence
FE-SEM	Field emission scanning electron microscope
LFO	$LaFeO_3$
LSFAl	$La_{0.2}Sr_{0.8}Fe_{0.8}Al_{0.2}O_{3\text{-}\delta}$
LSFTa	$La_{0.2}Sr_{0.8}Fe_{0.8}Ta_{0.2}O_{3\text{-}\delta}$
MIEC	Mixed ionic-electronic conducting
PEG	Poly(ethyleneglycol
PVA	Poly(vinylalcohol
PVP	Poly(vinylpyrrolidone
RD	Ruddlesden-Popper
SEM	Scanning electron microscope
Syngas	Synthesis gas, CO and H_2 gas mixture
T.p.c.	Total powder content
USF	Ultra sonic finger
Viz.	Videlicet (as follows)
XRD	X-ray diffraction

List of Figures

2.1 *Ideal perovskite structure with BO_6-octahedra and A-site cations placed in interstitial sites* 4
2.2 *Pseudo-binary phase diagram of $La_{1-x}Sr_xFeO_{3-\delta}$* 5
2.3 *Isothermal phase diagram of the ternary system $La_2O_3-SrO-Fe_2O_3$* 6
2.4 *Phase diagram of the $SrO-Al_2O_3$-system* 7
2.5 *Illustration of oxygen transport through a MIEC membrane* . . . 8
2.6 *Illustration of the oxygen flux profile versus membrane thickness* 10
2.7 *Illustration of an asymmetric membrane* 12

3.1 *Calcination program for solid state synthesis of LSFAl* 21
3.2 *Flow chart of the LSFAl2882 powder synthesis* 23
3.3 *Flow chart of LSFAl powder synthesis* 25
3.4 *Illustration of tape caster* 25
3.5 *Calcination program for the porous support, dip-coated once.* . . . 26
3.6 *Illustration of the thin functional layer ontop of the porous substrate after dip-coating.* 27
3.7 *Illustration of the dense functional layer ontop of the porous substrate after sintering. Densification has occured* 27
3.8 *Illustration of tape caster* 29

4.1 *SEM micrographs of the coarse LSFAl2882 powder. Note the different particle sizes* 31
4.2 *SEM micrographs of the carbon black powder used as a pore former after 30 minutes of ball milling. Note the many different shapes and sizes.* 32
4.3 *XRD-pattern of coarse LSFAl2882 powder: a) matched with LSF, and b) all present phases matched* 33
4.4 XRD-patterns: evolution of LSFAl2882 with temperature 34
4.5 XRD-patterns: Different compositions of LSFAl 36
4.6 *XRD-pattern of LSFAl2882 made with nano-alumina* 37
4.7 *Dilatometry curve for LSFAl2882* 38
4.8 *Particle size distribution of coarse LSFAl produced by the solid-state reaction* 38

4.9 *XRD-pattern of the sintered LSFAl porous support (support was crushed for XRD measurement)* 40
4.10 *XRD diagram of the calcined LSFAl powder and powder from the porous support (crushed after firing). Note the logaritmic y-axis* . 41
4.11 *SEM micrographs of porous support, a)-b) Cross sections, c)-d) top surface, and e)-f) bottom surface* 44
4.12 *Permeability coefficient of a porous support* 45
4.13 *Gas permeability of a porous support* 46
4.14 *Expected gas permeation of the porous support at elevated temperatures for different pressure drops.* 47
4.15 *Evolution of the Knudsen number with temperature, pressure held constant at* $\overline{p} = 1.005\text{bar}$. 47
4.16 *XRD-pattern of the sintered asymmetric membrane. The XRD measurement was done on the surface of the dense functional layer. Note the highligheted region (in red) exposing the presence of* $SrAl_2O_4$. 48
4.17 *SEM micrographs of the produced asymmetric membrane, a)-b) Cross sections, c)-e) dense layer surface (different magnifications)* 51
4.18 51
4.18 *SEM micrographs: comparing micrographs taken with the secondary electron detector and the backscatter detector* 52
4.19 *SEM micrographs: comparing micrographs of two asymmetric membranes* 52

5.1 *Comparison of the gas permeability of a porous support produced by tape casting (this work) and by uniaxial pressing (Wagner, N. [7])* 59
5.2 *SEM micrographs: comparing micrographs of two asymmetric membranes, dip-coated one and three times after the first firing* . 61
5.3 *SEM micrographs: comparing micrographs of two asymmetric membranes* 61
5.4 *SEM micrographs: comparing micrographs taken with the secondary electron detector and the backscatter detector* 62

F.1 *BET measurement data* XIV

G.1 *EDS analysis of the two seen phases from SEM micrograph* . . . XV
G.2 *EDS analysis of the dense layer of the asymmetric membrane* . . XVI

H.1 *Phase analysis by Topas* XXI

List of Tables

3.1 *Chemicals used for solid state synthesis* 17
3.2 *Additives used during green body preparation* 18
3.3 *Other chemicals used during experimental work* 19
3.4 *Apparatus used during membrane preparation* 20
3.5 *Amount of different precursors used for LSFAl 2882 powder synthesis, Batch 1* 22
3.6 *Amount of different precursors used for slip preparation.* 24
3.7 *Amount of precursors used to make the solution for spray-coating* 26

4.1 *Density of a coars LSFAl2882 green body before and after dilatometry* 37
4.2 *Powder surface area measured by nitrogen adsorption (BET)* . . 39
4.3 *True porosity of porous supports* 45
4.4 *Summary of permeation- and porous support parameters* 46

5.1 *Amount of the secondary* $SrAl_2O_4$*-phase in different* 54
5.2 *Expected permation at elevated temperatures* 58

A.1 *Cation radii* I

B.1 *LSFAl 2882, Batch 1* III
B.2 *LSFAl 2882, Batch 2* III
B.3 *LSFAl 2882, Batch 3* IV
B.4 *LSFAl 2882, Batch 4* IV
B.5 *LSFAl 4682, Batch 1* IV
B.6 *LSFAl 20808515, Batch 1* IV
B.7 *LSFAl 2882 with nano-sized alumina, Batch 1* V

D.1 *True porosity of porous supports* IX

Chapter 1

Introduction

The global demand for a cost effective, environmental friendly, and reliable source of pure oxygen is ever increasing. Dense ceramic membranes which exhibits mixed ionic and electronic conductivity (MIEC) properties at elevated temperatures ($T > 700°C$) have shown promising potential for oxygen separation from gaseous mixtures [1]. These membranes are 100 % selective towards oxygen and can possibly replace the conventional cryogenic technology by separating pure oxygen from e.g. air. MIEC materials are also suitable for other commercial applications such as electrodes in solid oxide fuel cells (SOFC) or as oxygen sensors. [1, 2, 3]. An application example of a MIEC-membrane can be to supply pure oxygen in the partial oxidation of methane to produce syngas [2], viz.:

$$CH_4 + \frac{1}{2}O_2 = CO + 2H_2, \qquad \Delta H = -36\frac{kJ}{mol} \tag{1.1}$$

When trying to decide suitable material systems for MIEC-membranes intended for e.g. syngas production, the material system must withstand very harsh operating conditions, such as: high operation temperatures, oxidizing and reducing atmospheres, and mechanical/chemical stress and strain. Therefore the material system must meet a number of requirements i.e. phase stability, dimensional stability/strength, avoid detrimental reactions in combination with other materials (compatibility), and show sufficient oxygen-ion and electron transport properties both with respect to bulk diffusion and surface exchange processes [1]. There are several material systems which could be suitable for these applications, but lately the most investigated systems in literature are materials based on the perovskite structure (ABO_3) [4].

The oxygen permeation flux through a MIEC membrane is governed by bulk oxygen ion diffusion and the surface exchange of oxygen between the membrane and the surrounding atmosphere. Depending on the thickness of the membrane either of these mechanisms can be rate limiting of the oxygen permeation through the membrane. The permeation in a thick membrane will be governed by bulk diffusion, whereas the permeation of a very thin membrane will be governed by surface exchange kinetics. [5]. From this it is quite obvious that the highest oxygen permeation flux is achieved by a thin membrane. When the membrane thickness decreases the need for a mechanical support becomes necessary to support the thin fragile membrane, and these composites are often called asymmetric membranes.

Asymmetric ceramic MIEC-membranes can be made from depositing a thin functional layer on one side of a porous support [3, 6]. In this work the porous support will be prepared from powder produced by the solid state reaction method. The support it self will be made by tape casting, and the dense functional layer will be deposited by dip-coating. The produced *asymmetric membrane* will then be further investigated for relevant properties i.e.: oxygen permeation; and phase stability. This thesis will focus on producing a porous support with one specific perovskite composition: $La_{0.2}Sr_{0.8}Fe_{0.8}Al_{0.2}O_{3-\delta}$ (LSFAl2882). This specific composition have shown promising potential regarding oxygen flux from previous studies done by Wagner, N. [7].

Chapter 2

Theory and Literature Review

2.1 Structure and Stability of Perovskite Type Oxides

The perovskite structure is one of the most promising crystalline structures for MIEC-membranes since their transport properties and stability in different atmospheres (oxidizing/reducing) varies over a wide range [4, 8]. The stability of a specific material is governed by many factors, especially when considering the harsh working conditions these membranes operate in. Of all the different stresses induced in the material during operation the most crucial seems to be the chemical strain resulting from the oxygen activity gradient in the sample. The stability is thus directly related to the amount of oxygen vacancies in the material. Therefore, as a general trend, the oxygen permeability and the stability of the perovskite materials show opposite tendencies, as they both are dependant on the oxygen vacancy formation/concentration. An oxygen separating membrane for commercial applications has to have a high oxygen permeability and sufficient chemical and structural stability. [1, 9, 10]

The ideal perovskite structure (ABO_3) consist of a BO_6-octahedra with A-site cations placed in interstitial sites, see Figure 2.1. The perovskite structure is very sensitive to the relative ion-size. Thus many materials, which are tailored for specific purposes, have a slightly distorted crystalline lattice from the ideal cubic lattice. Inducing oxygen vacancies by cation substitution will distort the ideal structure, and thus the stability of such tailored materials will vary from composition to composition [4].

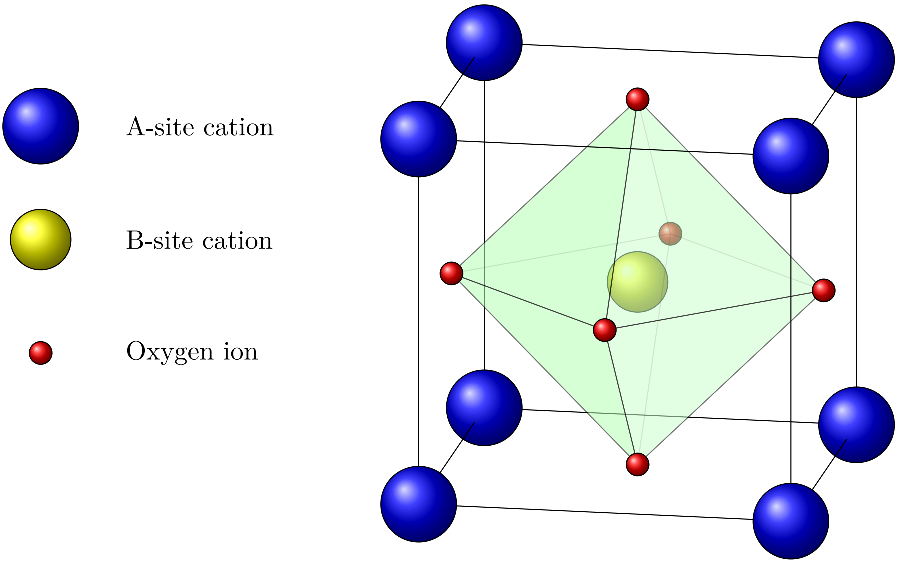

Figure 2.1: *Ideal perovskite structure with BO_6-octahedra and A-site cations placed in interstitial sites*

If the distortion becomes too large the material system will be exposed to stresses, and the symmetry of the perovskite can change from the ideal cubic ($Pm\overline{3}m$) symmetry to tetragonal (I4/mcm, P4/mbm), rhombohedral ($R\overline{3}c$, $Im\overline{3}$), or orthorombic (Pbnm, Pnma) symmetry. The relative amount of distortion of a perovskite can be calculated by the Goldschmidt tolerance factor (t_G) [11, 12, 13]:

$$t_G = \frac{r_A + r_O}{\sqrt{2}(r_B + r_O)} \tag{2.1}$$

where $r_{A/B/O}$ are the ionic radii of the A-site cation, B-site cation, and the oxygen ion respectively. For an ideal cubic perovskite the Goldschmidt tolerance factor is 1, whereas a tolerance factor which deviates from 1 represents a distorted structure due to ionic radii mismatch. The perovskite structure will exist, with different symmetry, for tolerance factor values ranging from $0.75 \leq t_G \leq 1.06$ [4].

In this work $LaFeO_3$ will be the host lattice for the material system $La_{0.8}Sr_{0.2}Fe_{0.8}Al_{0.2}O_{3\text{-}\delta}$ (LSFAl2882). $LaFeO_3$ doped with Sr^{2+} ($(La_{1\text{-}x}Sr_x)_yFeO_{3\text{-}\delta}$) have shown promising permeation results elsewhere [14, 15, 16]. The perovskite symmetry of $(La_{1\text{-}x}Sr_x)_yFeO_{3\text{-}\delta}$ is shown to vary with the amount of Sr^{2+}, and the pseudo-binary phase diagram of the system is shown in Figure 2.2 [13].

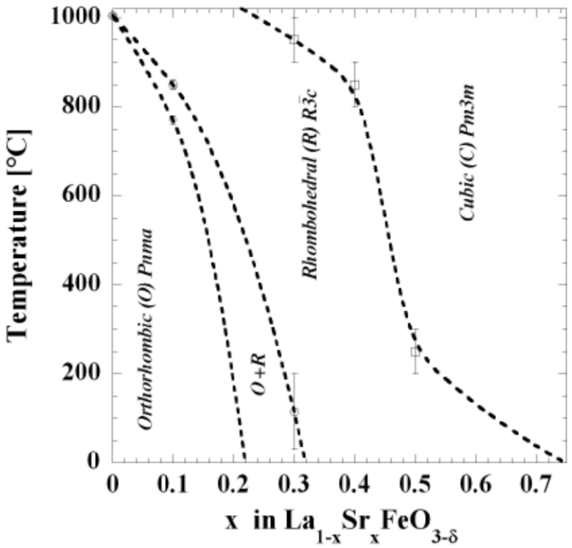

Figure 2.2: *Pseudo-binary phase diagram of* $La_{1\text{-}x}Sr_xFeO_{3\text{-}\delta}$*, Figure from [13]*

From Figure 2.2 it is seen that the system is cubic ($Pm\overline{3}m$) for $0.75 \leq x \leq 1$ at $0°C$. Generally, oxygen transport properties can be increased by substituting a lower valent cation into the lattice A-site [4]. By introducing the lower valent Sr^{2+}-ions at the A-site, and thus also introducing oxygen vacancies, the MIEC properties are suspected to increase. The system (LFO) can also cope with the incorporation of Sr^{2+}-ions by the partial oxidation of iron ($Fe^{3+} \rightarrow Fe^{4+}$) rather than introducing oxygen vacancies, and in reality a mix of these two mechanisms is expected to keep electron neutrality in the perovskite.

To increase the materials chemical stability Al^{3+}, which has a smaller ionic radii than $Fe^{3+/4+}$, can be substituted into the LSF lattice B-site. Thus changing the Goldschmidt tolerance factor of the material closer to unity. The Goldschmidt tolerance factor of LSFAl2882 has been calculated to: $0.987 \leq t_G \leq 1.01$, depending on the oxidation state of iron ($Fe^{3+/4+}$). For the same material system without B-site substitution ($La_{0.8}Sr_{0.2}FeO_{3\text{-}\delta}$) the Goldschmidt tolerance factor has been calculated to: $0.976 \leq t_{G_{LSF}} \leq 1.01$. From these calculations LSFAl2882 should be *closer* to the ideal cubic perovskite structure than LSF, regardless of the oxidation state of iron, see Appendix A for calculations.

The incorporation of Sr^{2+} into the lattice of $LaFeO_3$ can be represented in Kröger-Vink notation by the following equations, Viz.[10]:

$$SrFeO_3 \xrightarrow{LaFeO_3} Sr'_{La} + Fe^{\bullet}_{Fe} + 3O^{x}_{O} \tag{2.2}$$

With the bi-reactions:

$$2Fe^{\bullet}_{Fe} + O^{x}_{O} \quad \leftrightarrow \quad 2Fe^{x}_{Fe} + V^{\bullet\bullet}_{O} + \frac{1}{2}O_2 \tag{2.3}$$

$$2Fe^{x}_{Fe} \quad \leftrightarrow \quad Fe'_{Fe} + Fe^{\bullet}_{Fe} \tag{2.4}$$

The isothermal ternary phase diagram for the material system $La_2O_3-SrO-Fe_2O_3$ is given in Figure 2.3. From the figure it is seen that for the system to retain the perovskite structure the A/B-cation ratio must be equal to unity, and for LSFAl2882 this means that $(La_{1-x}Sr_x)/(Fe_{1-x}Al_x) = 1$.

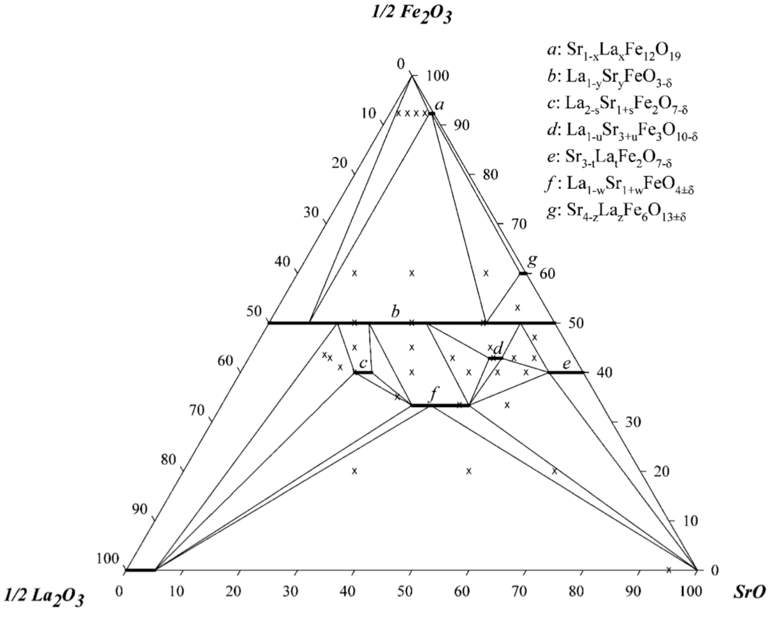

Figure 2.3: *Isothermal phase diagram of the ternary system $La_2O_3-SrO-Fe_2O_3$, from [17]*

The incorporation of Al^{3+} into the lattice of $LaFeO_3$ can be represented in Kröger-Vink notation by the following equation, Viz.[10]:

$$LaAlO_3 \xrightarrow{LaFeO_3} La_{La}^x + Al_{Fe}^x + 3O_O^x \tag{2.5}$$

The incorporation of Al^{3+} into LSF have shown from literature to yield some secondary $SrO-Al_2O_3$ phases [14, 18]. The phase diagram of the $SrO-Al_2O_3$-system is given in Figure 2.4.

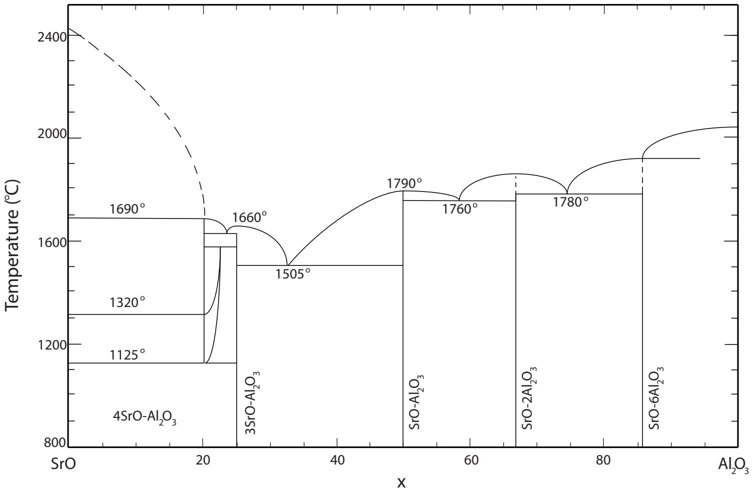

Figure 2.4: *Phase diagram of the $SrO-Al_2O_3$-system, Figure redrawn from [19]*

2.2 Oxygen Transport in Dense MIEC Membranes

The oxygen permeability through a MIEC membrane are mainly governed by two mechanisms.

1. Transport of oxygen ions through the bulk of the dense membrane layer. This transport is controlled by solid-state diffusion.

2. Rate of oxygen gas embodiment at the membrane surface, which is governed by surface exchange kinetics.

The main driving force for oxygen diffusion is the difference in chemical potential between the two active sides of the membrane. The chemical potential of oxygen is directly linked to the partial pressure of oxygen, and thus the operation principle for a MIEC-membrane can be explained as the diffusion of oxygen through the materials crystal lattice as a result of difference in the oxygen partial pressure between the two membrane sides [1, 2, 4]. This process is illustrated in Figure 2.5, where a MIEC-membrane supplies pure oxygen in the partial oxidation of methane gas.

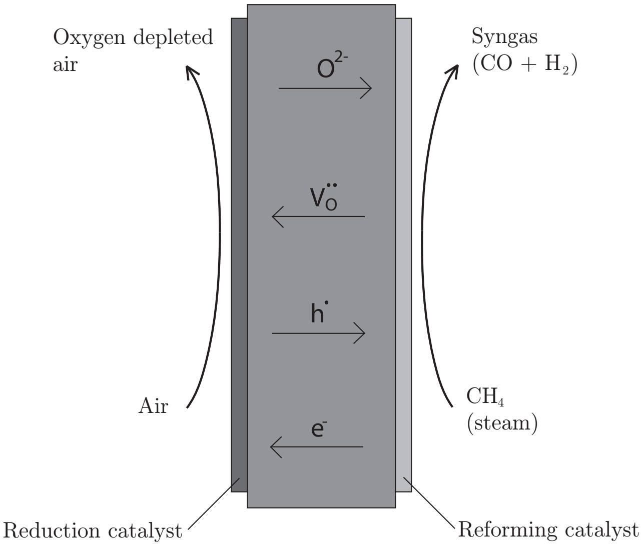

Figure 2.5: *Illustration of oxygen transport through a MIEC-membrane in the partial oxidation of methane to produce syngas, Figure redrawn from [1] .*

Bulk Diffusion

Bulk diffusion, which is the rate ions move through the solid matrix (crystal lattice), is a well studied and understood mechanism. The phenomena can be explained by Wagner theory, and the Wagner equation relates the bulk diffusion of oxygen through a dense sample to the materials ionic/electronic conductivity and the partial pressure difference between the two membrane sides, Viz. [20].

$$j_{O_2} = \frac{-RT}{4^2F^2L}\int_{ln(p'_{O_2})}^{ln(p''_{O_2})} \frac{\sigma_{el}\sigma_{ion}}{\sigma_{el}+\sigma_{ion}} dln(p_{O_2}) \tag{2.6}$$

where R is the universal gas constant; F is the Faraday constant; L is the membrane thickness; p'_{O_2} and p''_{O_2} are the partial pressures of oxygen at the high- and low p_{O_2} side of the membrane respectively; σ_{el} and σ_{ion} are the electronic and ionic conductivity respectively. The driving force for diffusion through the membrane is the difference in the chemical potential of oxygen between the two membrane sides. Oxygen will diffuse through the membrane from the high p_{O_2} side to the low p_{O_2} side. This is typically done by introducing air at one side, and a reducing gas at the other side [1].

To satisfactory describe a permeable membrane system two coefficients are introduced. The chemical diffusion coefficient, D_{chem}, and the surface exchange coefficient, k_{chem}. From literature it is shown that the ratio between these two coefficients represents the critical thickness, L_C, which indicates the shift between the two rate determining mechanisms mentioned [5, 16].

$$L_C = \frac{D_{chem}}{k_{chem}} \tag{2.7}$$

When the thickness of the dense membrane layer, $L < L_C$: Surface exchange rate is the limiting factor of j_{O_2} and thus no further increase of j_{O_2} will occur without increasing the surface exchange rate. When $L > L_C$: Diffusion through the bulk is the rate limiting factor of j_{O_2} and an increase in flux is only possible by reducing L $(L \rightarrow L_C)$ or by increasing Δp_{O_2}. Lastly when $L = L_C$ there is an equilibrium between the two mechanisms. The oxygen flux profile as a function of the inverse membrane thickness is illustrated in Figure 2.6, which illustrates that the flux reaches a maximum when surface exchange kinetics takes over as the rate determining mechanism.

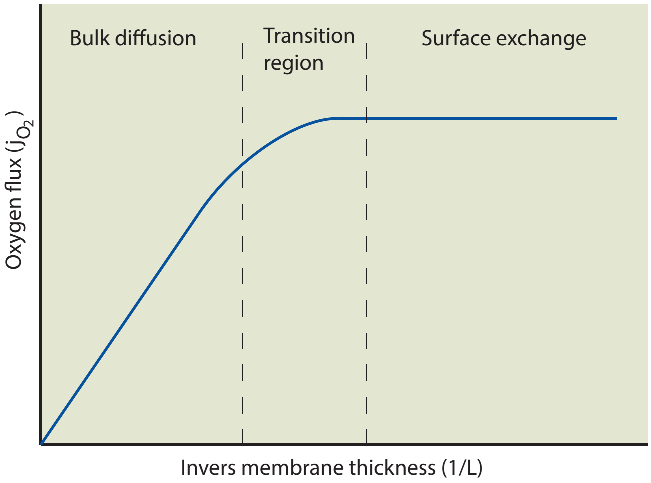

Figure 2.6: *Illustration of the oxygen flux profile versus membrane thickness*

Oxygen Surface Exchange

Oxygen surface exchange is the process when oxygen gas is adsorbed into the crystal lattice of the material. The total reaction which describes the exchange of oxygen between the membrane surface and the ambient atmosphere is given in Equation 2.8 (Kröger-Vink notation) [12].

$$\frac{1}{2}O_2(g) + V_O^{\bullet\bullet} + 2Fe_{Fe}^{x} = O_O^{x} + 2Fe_{Fe}^{\bullet} \tag{2.8}$$

The rate determining mechanism for the total process is not fully understood, but from literature it is suggested that the rate determining step is the dissociation and adsorption of $O_{2_{(g)}}$ on an oxygen vacancy in the lattice at the high p_{O_2} side of the membrane [21].

The surface exchange of oxygen can be described as a flux of oxygen in or out of the sample, depending on if it is a oxidation- or reduction reaction. When the fluxes in and out of the sample are equal there is no driving force for surface exchange, and the net oxygen flux is zero. However if there is a change in the chemical potential (partial pressure) of oxygen in the ambient atmosphere there will be a net flow of oxygen either in or out of the sample. One way to express this relation is to introduce the chemical diffusion- and surface exchange coefficient, as done by Watterud [12]:

$$j_{O_2} = \frac{-D_{chem}}{2}\frac{dC_O}{dx}\bigg|_{surface} = \frac{k_{chem}\Delta C_O}{2} \tag{2.9}$$

where ΔC_O is the difference in concentration of atomic oxygen at the membrane surface between two equilibrium states. From the above equation it can be concluded that the flux of oxygen through a thin dense membrane only can be increased by increasing k_{chem} which can be done by e.g. surface structuring. The improvement of oxygen flux by surface structuring was shown by the Author in previous work [22].

2.3 Asymmetric Membranes

When making thin dense membranes several potential problems must be taken into consideration. The handling of such thin membranes become impossible without mechanical failure, therefore the need of a membrane support is essential. Since the operating temperature of the oxygen separation membranes are $T \geq 700°C$ the support material should have a similar thermal expansion coefficient to the thin dense functional layer (membrane). Thus a porous support made from the same material as the thin dense layer is the best option since they will have the same thermal expansion during heating/cooling. An illustration of a thin dense layer on-top of a porous support is shown in Figure 2.7.

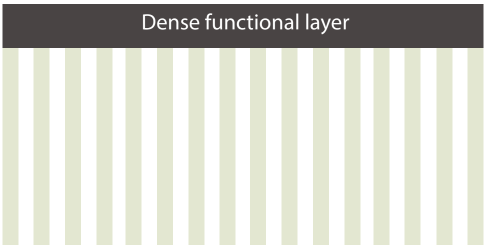

Figure 2.7: *Illustration of an asymmetric membrane showing the dense functional layer ontop of a porous support (Note: not in scale)*

The gas flow properties of the porous support are also important, especially since the gas mixture must get to the dense functional layer before any oxygen separation can occur. Therefore the porous support should be as thin as possible, have as much open/connected porosity as possible, and also have sufficient mechanical strength so that the asymmetric membrane can be handled with ease. The preferred route to make porous ceramics is by introducing an organic component, which acts as a pore former, into the green body which burns off and leaves pores during firing. Several different organic pore formers are available, however in this work activated charcoal (carbon black) is the pore former used during all experiments as it has shown promising results elsewhere [7, 22, 23].

2.3.1 Gas Flow in Porous Materials

Since the purpose of the MIEC-membranes is to separate oxygen from a gaseous mixture it is important that the flow of gas in the porous support allows for gas flow both into and out from the dense functional layer. This is to avoid build up of other gas species on the membrane surface which effectively will kill, or severely limit, the rate of oxygen diffusion. Generally gas flow in a porous material can be divided into two main regimes:

1. **Knudsen regime** Knudsen diffusion is the phenomena when diffusion no longer appears as a continuum of moving molecules, but rather random flow governed by molecule-wall interactions. This occurs when the mean free path of the gas molecule is longer than the pore size, and thus the gas molecules can move independently of each other. The driving force for Knudsen diffusion is the concentration gradient of the species along the pore [24].
2. **Continuum regime** In the continuum regime gas flow is characterized by molecule-molecule interactions, and can thus be looked upon as a continuum rather than movement of single molecules. In the continuum regime the pore size is substantially larger than the mean free path of the gas molecules. The diffusion of gas in this regime is a mix of continuum diffusion and viscous gas flow. Continuum diffusion is controlled by concentration gradients, whereas viscous flow is non-separating bulk flow controlled by the total pressure gradient across the porous material [24].

From the mentioned mechanisms viscous gas flow is the preferred, as the driving force comes from the pressure gradient across the bulk. For viscous flow to occur, and be dominating, the porous support should have good connected porosity, thus increasing the ratio between the pore size and the mean free path of the gas molecules. From literature the Dusty Gas Model (DGM) has been used to describe transport in porous materials [25, 26]. The general DGM is given by [24]:

$$\frac{RT}{D_{iK}}J_i + \sum_{j=1}^{n}\left[\frac{RT}{D_{ij}}(x_jJ_i - x_iJ_j)\right] = -\bigtriangledown p_i - \frac{x_i}{D_{iK}}\frac{\beta_0 p}{RT\mu}\bigtriangledown p \tag{2.10}$$

where D_{iK} and D_{ij} are the Knudsen- and continuum diffusion coefficients, respectively, given as:

$$D_{iK} = \frac{4}{3}K_0\nu_{Mi} \tag{2.11}$$

and

$$D_{ij} = \frac{\epsilon}{\tau}d_{ij} \tag{2.12}$$

furthermore J_i is the molar flux of component i, x_i is the mole fraction of component i, $\bigtriangledown p_i$ is the partial pressure drop across the membrane of component i, $\bigtriangledown p$ is the total pressure drop across the membrane, β_0 is a geometric factor characteristic of the porous medium and is independent of the gas used, μ is the gas viscosity, K_0 is a morphological parameter of the Knudsen diffusion coefficient, ν_{Mi} is the mean molecular speed of component i, ϵ is the porosity,

τ is the tortousity, and d_{ij} is the intrinsic binary diffusion coefficient [24]. This theory goes beyond the scope of this work, but is mentioned due to the complex nature of gas flow in porous media and to show that one cannot simply assume that one mechanism dominates over another without either running simulations or doing experimental work.

2.3.2 Permeability of Porous Materials

The permeability of a porous material must not be confused with the permeability of e.g. oxygen through a dense membrane (solid-state diffusion). Gas permeability through a porous material will depend strongly on the pore geometry. If a material only has closed porosity the gas permeability will be non excisting, whereas if the material has open/connected porosity across the whole bulk gas permeability is expected to occur. The amount of connected porosity in a material is often expressed as the degree of tortuosity, Viz:

$$\tau = \frac{L_p}{h} \tag{2.13}$$

where τ is the degree of tortousity, L_p is the actual path length of a pore, and h is the porous materials thickness. The gas permeability of a porous material can be described by the pressure dependent permeation coefficient, K, from the following relation [27, 28]:

$$J(T,p) = K(T,p)\frac{\Delta p}{l} \tag{2.14}$$

where Δp is the pressure drop across the porous material and l is the thickness of the porous support. Furthermore K is given as [28]:

$$K(T,p) = K_0 + \frac{B_0}{\eta(T)}\overline{p} \tag{2.15}$$

where K_0 is the Knudsen permeability coefficient, B_0 is the geometric factor of the porous material, $\eta(T)$ is the gas viscosity at a given temperature, and $\overline{p}$ is the mean pressure ($\overline{p} = (p_1 + p_2)/2$). By plotting K *vs.* $\overline{p}$ the Knudsen permeability coefficient, K_0, and $B_0/\eta(T)$ can be determined. Another approach to determine the gas permeability is using Darcy's law. This equation can only be used if one assumes that the Knudsen diffusion is zero such that viscous flow is the only contributing mechanism for gas flow [29]. Darcy's law is given as [30]:

$$Q_{Darcy} = \frac{D \cdot A \cdot \Delta p}{\eta(T) \cdot l} \tag{2.16}$$

where Q_{Darcy} is the volumetric flow, D is the permeability (m^2) usually presented in either nano-Perm (nPm) or Darcy, where $1\ nPm = 10^{-13}\ m^2$ and $1\ Darcy = 9.872\ nPm$.

Flow regimes can also be classified based on the Knudsen number (Kn). Generally one can safely assume that the continuum regime applies if $Kn < 0.01$, and that the Knudsen regime fully takes over as the transport mechanism when $Kn > 10$. Between these two limits there is a mixture of both flow regimes (transition flow) [29]. The Knudsen number can be calculated from [29]:

$$Kn(T,p) = \frac{\lambda(T,p)}{r} \tag{2.17}$$

where $\lambda(T,p)$ is the mean free path of the permeating gas at a given temperature and pressure, and r is the throat pore radius. $\lambda(T,p)$ is given as:

$$\lambda(T,p) = \frac{k_B T}{\sqrt{2}\pi d^2 p} \tag{2.18}$$

where k_B is the Boltzmann constant, d is the diameter of the gas molecule, and p is the pressure. The throat pore radius can be calculated from a modified version of Darcy's law as proposed by Ziarani et.al. with the same assumption that viscous flow is the only contributing mechanism for gas flow [29]:

$$Q_{Darcy} = \frac{\pi r^4}{8\eta} \frac{\Delta p}{l} \tag{2.19}$$

where r is the throat pore radius. Rearranging Equation 2.19 gives a expression for the throat pore radius [29]:

$$r = \sqrt[4]{\frac{8 Q_{Darcy} \eta l}{\pi \Delta p}} \tag{2.20}$$

Chapter 3

Experimental

3.1 Chemicals and Apparatus

3.1.1 Chemicals

LSFAl2882 was synthesised by the solid state reaction method. The precursors, their formula, suppliers, and purity can be seen in Table 3.1.

Table 3.1: *Chemicals used for solid state synthesis*

Chemical	**Formula**	**Supplier**	**Purity**
Lanthanum(III)oxide	La_2O_3	Merck KGaA	99 wt%
Strontium carbonate	$SrCO_3$	Alfa Aesar GmbH Co.KG	99.4 wt%
Iron(III)oxide	Fe_2O_3	VWR International AS	99 wt%
Aluminium(III)oxide	Al_2O_3	Alfa Aesar GmbH Co.KG	99.99 wt%
Ethanol	CH_3CH_2OH	VWR International AS	$\geq$99.8 vol%

During the green body preparation several chemical additives were used to stabilize and give functional properties to the slip before tape casting. A list of the additives and chemicals used, their supplier, and their purpose can be seen in Table 3.2

Table 3.2: *Additives used during green body preparation*

Name	**Supplier**	**Purpose**
Activated charcoal	Merck KGaA	Pore former
BYK 3455	BYK-chemie GmbH	Wetting agent
PVA	Merck	Binder
PVP	Alfa Aesar	Surfactant
PEG 400	Merck	Plasticizer
Dolacol D 1003	Zschimmer & Schwarz GmbH	Surfactant

Other chemicals used during this thesis work can be seen in Table 3.3

3.1.2 Apparatus

During the preparation and analysis of the samples made during this work different apparatus were used. Table 3.4 lists the type, model name, manufacture, and area of use.

Table 3.3: *Other chemicals used during experimental work*

Chemical	**Formula**	**Supplier**	**Purity**	**Purpose**
LSFAl2882	$La_{0.2}Sr_{0.8}Fe_{0.8}Al_{0.2}O_3$	CerPoTec AS	99 wt%	Dense functional layer
Stearic Acid	$CH_3(CH_2)_{16}COOH$	Made at NTNU	-	Lubrication
Reagent grade ethanol	CH_3CH_2OH	Sigma Aldrich	$\geq$ 99.8 vol%	Solvent
Ethanol	CH_3CH_2OH	Sigma Aldrich	$\approx$ 96 vol%	Solvent/cleaning aid

Table 3.4: *Apparatus used during membrane preparation*

Type	Model name	Manufacture	Area of use
Furnace	Entech HT2 Chamber furnace	Entech	Sintering
	Entech SF4 Chamber furnace	Entech	Calcination
	Nabertherm P330	Nabertherm	Calcination
SEM	LVFESEM Zeiss Supra, 55 VP	Carl Zeiss	Sample characterization
	LVSEM Hitachi S-34000N	Hitachi	Sample characterization
XRD	AXS D8Focus	Bruker	Phase composition
USF	Branson Digital Sonifier	Emerson	Ultrasonic stirring
Planetary Mill	Retsch PM 100	Retsch	Mixing and crushing of powder
Rotary Evaporator	Buchi Rotavapour	Buchi	Removing solvent from powder
Particle Size	Malvern Mastersizer 2000	Malvern	Particle size distribution
Dilatometry	DIL 402 PC	Netzsch	Measuring sintering behaviour
Permeability	-	Gurauskis et Al.	Air permeation measurements

3.2 Procedure

3.2.1 LSFAl powder synthesis

The synthesis of the coarse LSFAl2882 powder used in the porous support production was done by a solid state reaction. The oxide precursors for this reaction (La_2O_3, Fe_2O_3, and Al_2O_3) were calcined (800°C, 12 h, ±200°Ch^{-1}) in three different crucibles (Al_2O_3) and taken out from the furnace at 200°C. The calcined oxides and $SrCO_3$ were immediately weighed out in the right stoichiometric amounts in a ZrO_2-container (250 mL). Ethanol (100%, 150 mL) was added as a wetting agent. The compounds were mixed by planetary mill (70 ZrO_2 balls, Ø = 10mm, 150 rpm, 1 h). After mixing the slurry was dried by rotavapor (65 mbar, 1.5h). The powder was further dried by putting it on a heater (150°C, 10 min) to remove any ethanol residue. The dried powder mixture was transferred into a alumina crucible for calcination (1200°C, 12h, ±200°Ch^{-1}). The finished coarse LSFAl2882 powder was milled by planetary mill to obtain the right particle size distribution. The heat program used for calcination can be seen in Figure 3.1

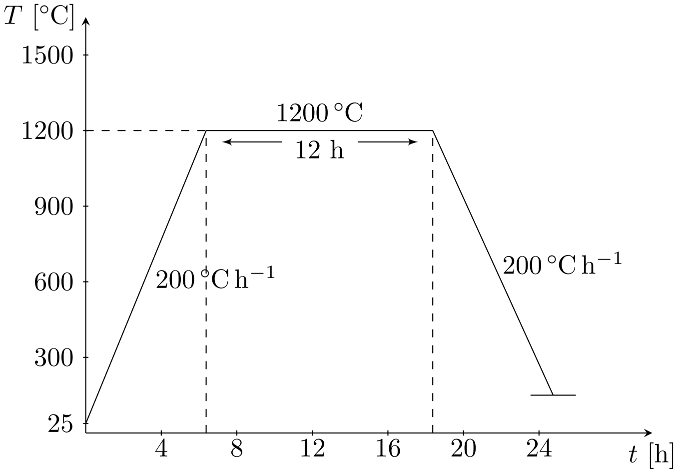

Figure 3.1: *Calcination program for solid state synthesis of LSFAl*

A flow chart of the LSFAl solid state synthesis procedure can be seen in Figure 3.2, and the amount of calcined oxides and as received $SrCO_3$ used in the LSFAl2882 powder synthesis of one of the prepared batches can be seen in Table 3.5. The amount of precursors used to prepare all the different batches made during this work can be seen in Appendix B.

Table 3.5: *Amount of different precursors used for LSFAl 2882 powder synthesis, Batch 1*

Chemical	**Amount [g]**	**mole%** [1]
La_2O_3	14.385	10
$SrCO_3$	52.095	40
Fe_2O_3	28.205	40
Al_2O_3	4.498	10
Total	99.183	100

---

[1] Calculations given in Appendix C

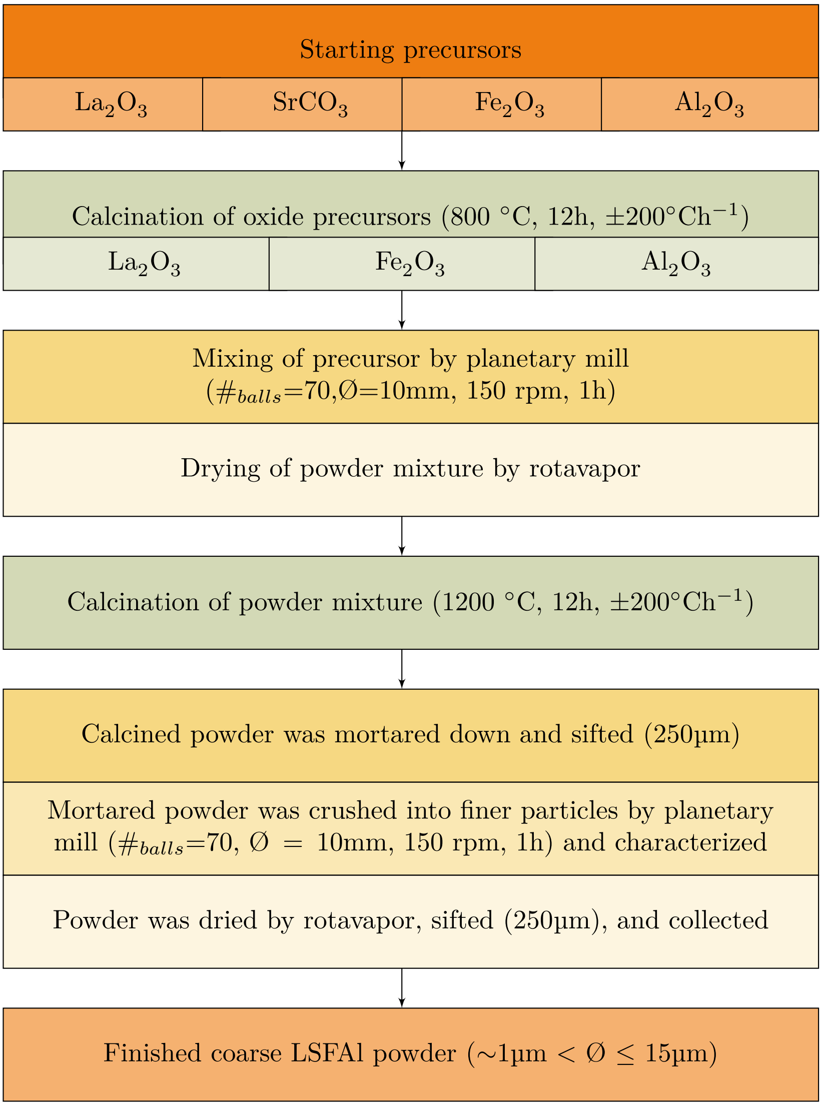

Figure 3.2: *Flow chart of the LSFAl2882 powder synthesis*

3.2.2 Production of Porous Support

The porous support was produced by tape casting. Before the slip could be made a BET-analysis was done one the raw powder to obtain the surface area per unit mass $[m^2 \cdot g^{-1}]$. The obtained surface area was then used to adjust the amount of surfactant to powder ratio. The amount of the different precursors used during slip preparation can be seen in Table 3.6. The procedure for slip preparation can be seen in Figure 3.3, and a illustration of the tape caster can be seen in Figure 3.4.

Table 3.6: *Amount of different precursors used for slip preparation. T.p.c = Total powder content*

Chemical	Amount [g]	Remarks	Purpose
$LSFAl_{2882}$	22.700	60 vol% of t.p.c.	Support material
CarbonBlack [2]	6.000	40 vol% of t.p.c.	Pore former
Water	27.3	100 vol% of CB	-
PVA	4.305	15 wt% of t.p.c.	Binder
PEG400	3.875	90 wt% of PVA	Plasticizer
PVP	0.0778	0.0032 g/cm^2 of LSFAl2882	Surfactant
BYK 3455	0.6664	0.7 wt% of total slip	Adjust surface tension of slip

---

[2] Carbon Black was pretreated with PVP (2 wt% of CB)

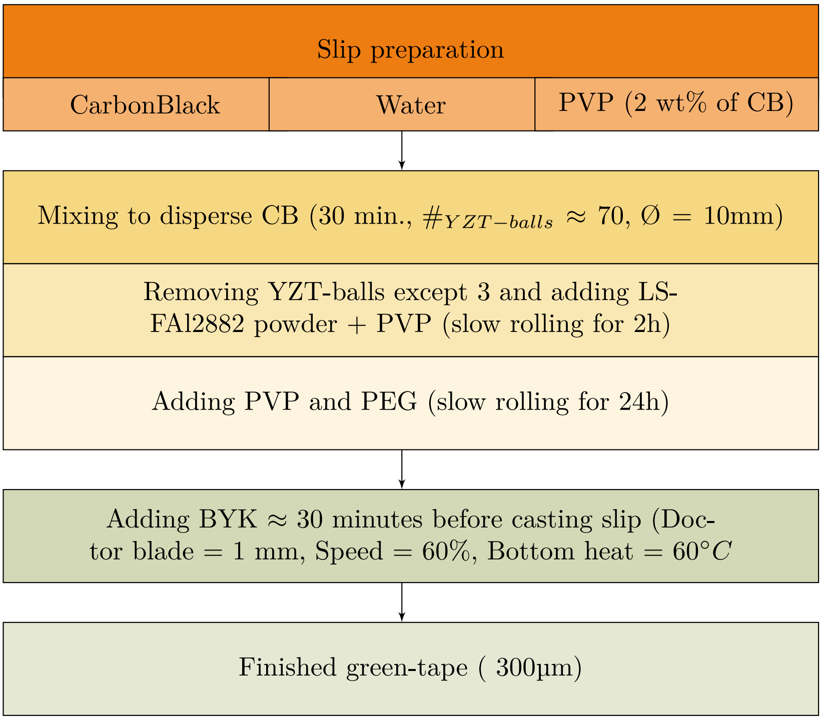

Figure 3.3: *Flow chart of LSFAl powder synthesis*

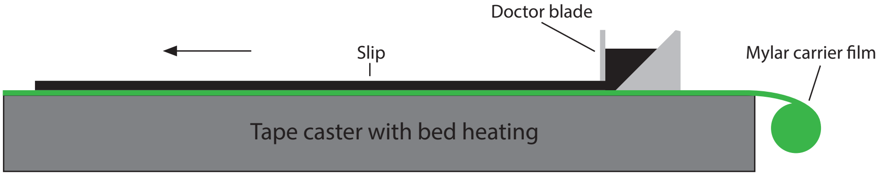

Figure 3.4: *Illustration of operating principle for a tape caster*

From the finished green-tape, disk-shaped green bodies (Ø = 30mm) were made with a pressing tool. The wanted thickness for the porous support was around 1 mm, and six disk-shaped green bodies were laminated together by utilizing an hot-press ($75°C$, 2 $tonf/cm^2$, 5 min) to produce the final green body for the porous support.

3.2.3 Applying Dense Functional Layer

A dense functional layer of fine LSFAl2882 powder (spray pyrolysed) was applied to the green body produced according to the method described in Section 3.2.2. The dense functional layer was applied by dip-coating. The dip-coating suspension was made with precursors according to Table 3.7. Grinding balls (Al_2O_3, $\varnothing = 5$mm) was added and the suspension was ball milled for homogenization for 24 hours. After 24 hours the suspension was diluted 1:4 to make the final 0.5 vol% suspension. Before dip-coating the green body the suspension was homogenized by ultrasound. After the appliance of said layer the asymmetric membrane was calcined according to Figure 3.5. An illustration of both the porous support and the thin dense functional layer (before sintering) can be seen in Figure 3.6.

Table 3.7: *Amount of precursors used to make the solution for spray-coating*

Chemical	**Amount [g]**	**Remarks**	**Purpose**
LSFAl	2.5	2.5 vol%	Dense layer
EtOH	16.962	-	Solvent
Dolacol D 1003	0.0563	2.25 wt% of LSFAl	Surfactant

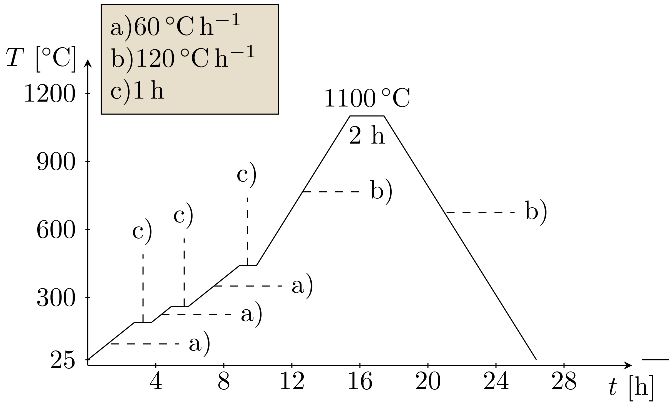

Figure 3.5: *Calcination program for the porous support, dip-coated once.*

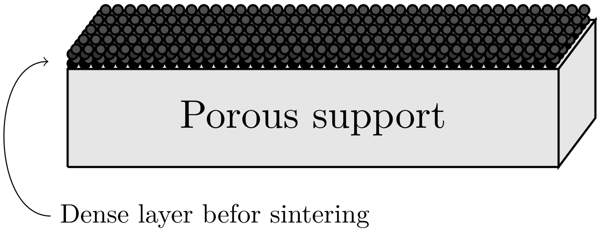

Figure 3.6: *Illustration of the thin functional layer ontop of the porous substrate after dip-coating.*

After the first firing three additional dense layers were applied by dip-coating (5 minutes between each dip-coating) to be certain of producing a gas tight functional layer. The asymmetric membrane was sintered (1400°C, 4 h, $\pm 120^{\circ}\mathrm{Ch}^{-1}$), and a illustration of the asymmetric membrane after the final sintering, when the thin functional layer has densified, can be seen in Figure 3.7.

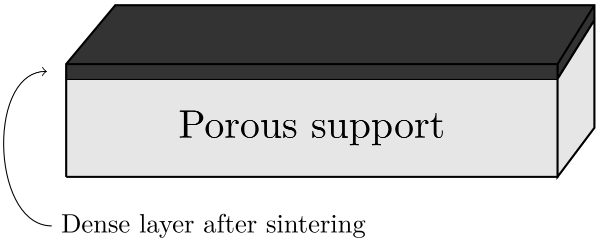

Figure 3.7: *Illustration of the dense functional layer ontop of the porous substrate after sintering. Densification has occured*

3.3 Characterization of Powder and Membrane Properties

Several different characterization techniques were utilized during this work, a short summery of the different techniques and program settings are given in the subsequent sections.

3.3.1 Phase Determination

Phase determination of powders and samples was done by X-ray powder diffraction (XRD) on a Burker D8Focus set up to use Bragg-Brentano geometry for analysis. The XRD-patterns shown in this work was recorded in θ-range $20° \leq \theta \leq 60°$ using CuK$_\alpha$-radiation. Step size for all samples was 0.01° and the collection time was 0.2 s.

3.3.2 Particle Size Distribution and Surface Area Determination

Particle size distribution of the LSFAl powder made by the solid state reaction was done on a Malvern Mastersizer 2000. The principle behind the measurement is dynamic light scattering [31]. Standard program settings was used during analysis and each sample was measured 3 times and the software calculated the average particle size distribution.

The surface area of the LSFAl powder prepared by the solid state reaction was measured using a Micromeritics^{TM}Tristar 3000. The surface area of the powder is calculated by the software using BET-theory (adsorption of N_2-gas on the powder surface)

3.3.3 Linear Shrinkage

The shrinking behavior of the prepared powder was studied using dilatometry. A LSFAl-rod ($\O = 5mm, L = 5-15mm$) made from powder from the solid state reaction (Section 3.2.1) was placed in the instrument (NETSCH DIL 402C) with a heating rate of $2K/min$ up to $1400°C$. The sample was exposed to synthetic air during the measurement, and the recorded data was used to determine the sintering program used throughout this work.

3.3.4 Density and Porosity Determination

The relative density of a densely packed green body before and after sintering was measured using sample geometry and weight. The true porosity of the porous supports was measured by the ISO standard: *ISO-5017:1998 - Determination of bulk density, apparent porosity, and true porosity.* Calculations of the true porosity can be seen in Appendix D. The theoretical density of LSFAl2882 used in this work is 5.54 g·cm^{-3}, as stated by Phung [32].

3.3.5 Morphology by SEM

SEM micrographs seen in this work were taken on either an Hitachi S-3400N LVSEM, Zeiss Supra55 LVSEM, Zeiss Supera55 FESEM. Voltage and magnification settings are visible in each micrograph. Samples were placed on sample holders by either tacky carbon tape or carbon glue. No conducting coating of the samples were necisarry because LSFAl is electronically conductive.

3.3.6 Porous Support Permeability Measurements

The air permeability of the porous support was measured by mounting the porous support on a tube and measuring the overpressure (P_1^*) inside the tube, and the flow rate of gas permeating through the sample. From these measured values the air permeability of the porous support was determined according to the theory in Section 2.3.2. A illustration of the experimental setup can be seen in Figure 3.8

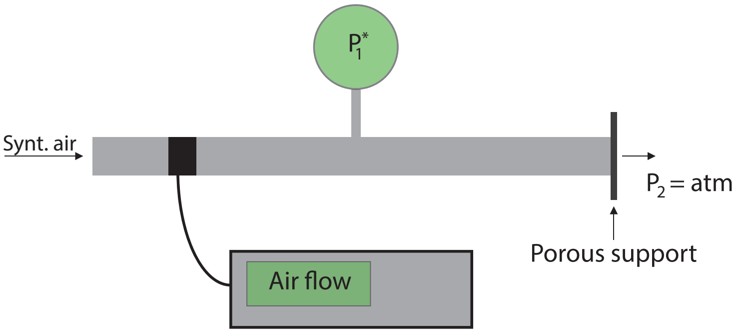

Figure 3.8: *Illustration of experimental setup for air permeation measurements of the porous supports*

Chapter 4

Results

4.1 LSFAl Powder Synthesis

4.1.1 Particle Morphology

The morphology of the LSFAl2882 powder was investigated by SEM and the micrographs can be seen in Figure 4.1

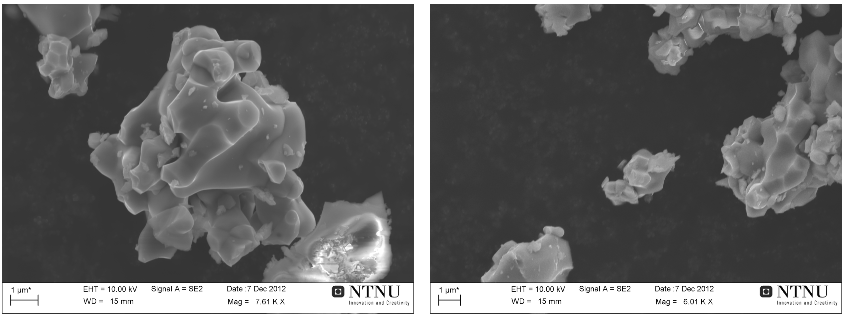

(a) **(b)**

Figure 4.1: *SEM micrographs of the coarse LSFAl2882 powder. Note the different particle sizes*

Furthermore the morphology of the carbon black powder (milled for 30 minutes) used as a pore former during tape casting can be seen in Figure 4.2

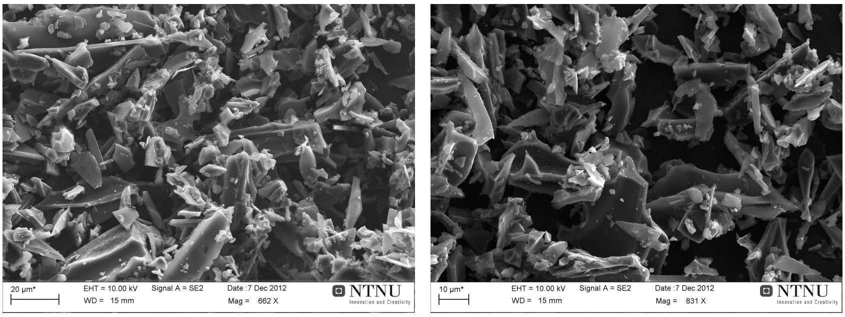

(a) Carbon Black **(b)** Carbon Black, note the different scale

Figure 4.2: *SEM micrographs of the carbon black powder used as a pore former after 30 minutes of ball milling. Note the many different shapes and sizes.*

4.1.2 Phase Purity

LSFAl2882 powder was produced according to Section 3.2.1. The XRD-pattern of the powder used for porous support production can be seen in Figure 4.3(a).

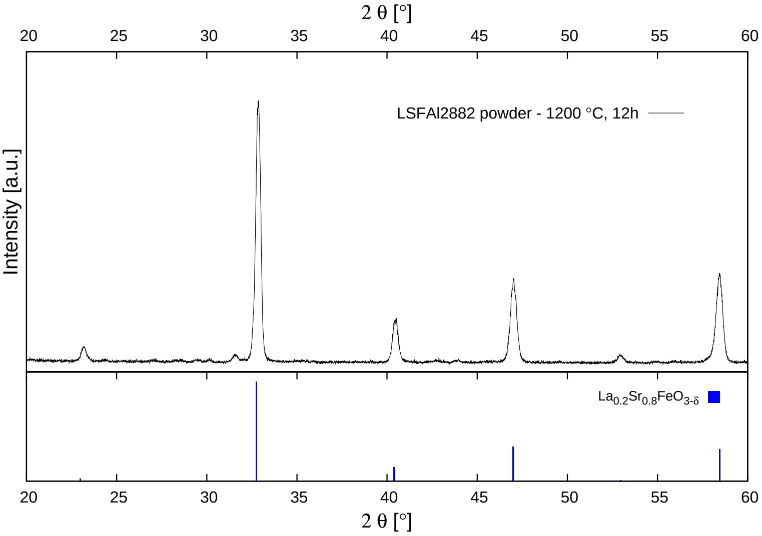

(a) XRD-pattern of coarse LSFAl2882 powder: matched to cubic LSF

As seen from the XRD-pattern in Figure 4.3(a) the powder consists mostly of a single perovskite phase, however there are traces of secondary phases present. The XRD-pattern was matched to the ICDD PDF-4+ database[1]to try and determine the other phases. From this search two distinct phases seemed to be present: The spinel phase $SrAl_2O_4$ and the Ruddlesden-Popper (RD) type phase $(LaSr)_2FeO_4$ matched well to the undistinctive peaks found in the XRD-pattern of the calcined powder, see Figure 4.3(b).

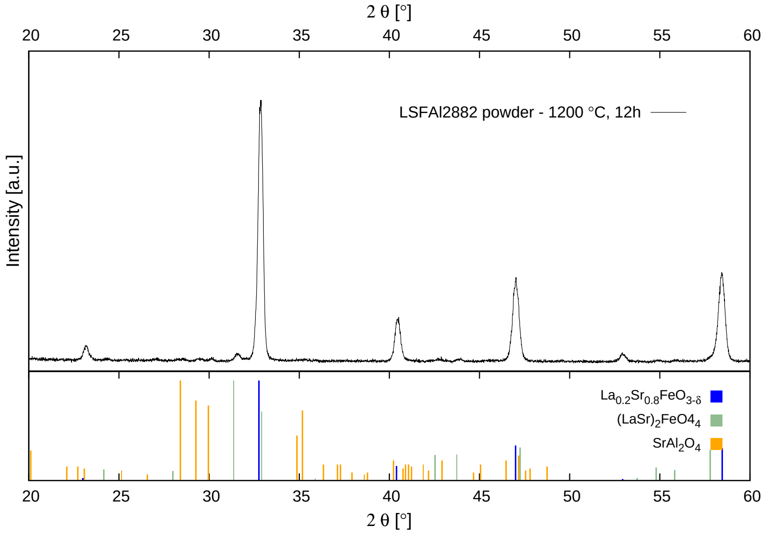

(b) XRD-pattern of coarse LSFAl2882 powder: All undistinctive LSF peaks matched. Note: logarithmic scale on the y-axis

Figure 4.3: *LSFAl2882 powder with matched phases* [2]

Phase Study of LSFAl

As a result of the finding of secondary phases a short study of different firing temperatures was done to try and remove them, and in Figure 4.4 the development of the XRD-pattern as the temperature increases, can be seen.

---

[1] All XRD-patterns was matched with the ICCD PDF-4+ database [33]

[2] The XRD-pattern are from the main powder batch, see Table B.4 in Appendix B

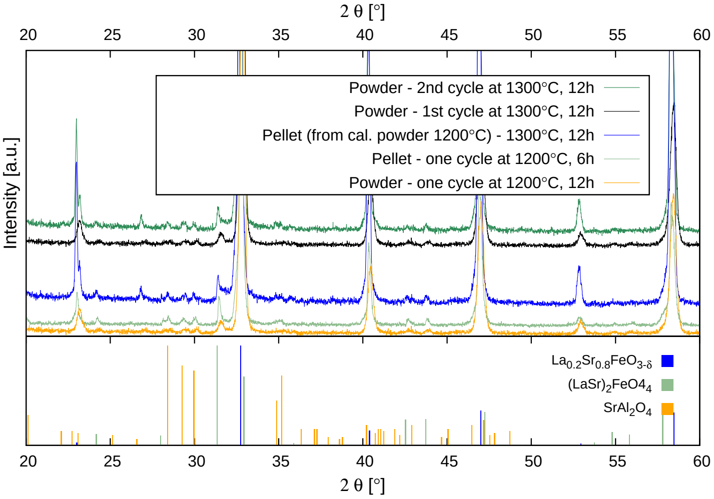

(a) XRD-pattern: Evolution of LSFAl2882 powder with temperature

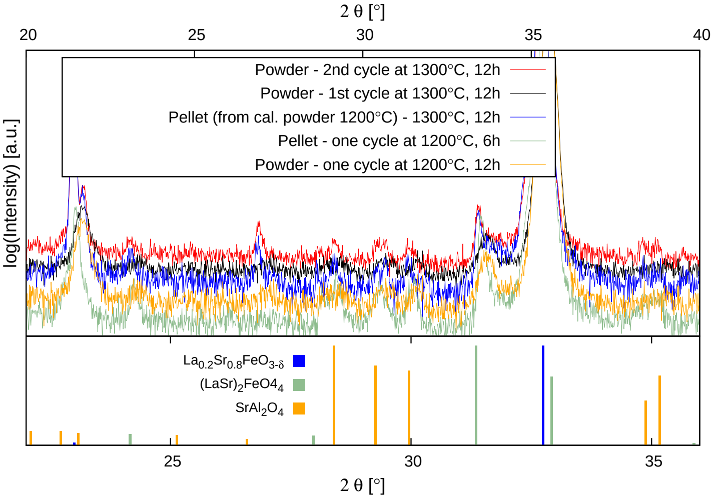

(b) XRD-pattern: Evolution of LSFAl2882 powder with temperature. Note the logscale on the y-axis and the reduced 2θ area.

Figure 4.4: *XRD-patterns: evolution of LSFAl2882 with temperature*

As seen from Figure 4.4 the mentioned secondary phases ($SrAl_2O_4$ and $(LaSr)_2FeO_4$) are present in all the different XRD-patterns. The phases did not diminish or evolve further (in any notable way) with the different firing temperatures used to prepare the calcined LSFAl2882 powder.

Since LSFAl2882 was not prepared phase pure by the solid-state reaction in this work, even when considerable effort was put into producing a phase pure powder, different compositions of LSFAl was prepared to see if the composition of the different cations played part in producing a phase pure powder. In Figure 4.5 the XRD-pattern for two different LSFAl compositions can be seen.

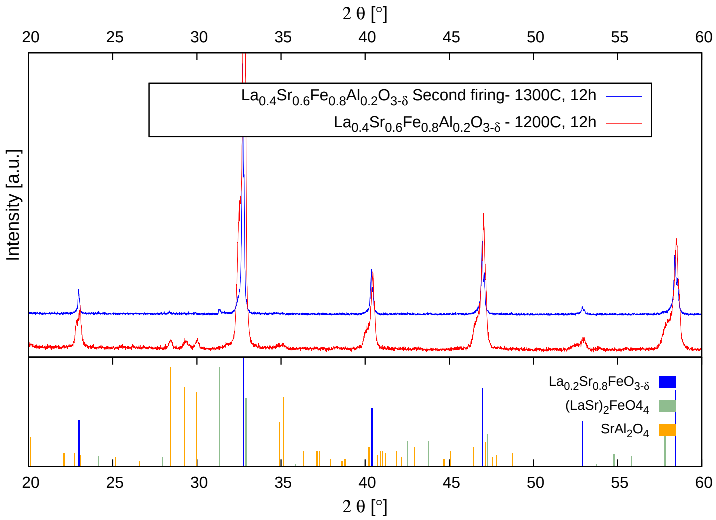

(a) XRD-pattern: LSFAl4682 evolution with temperature

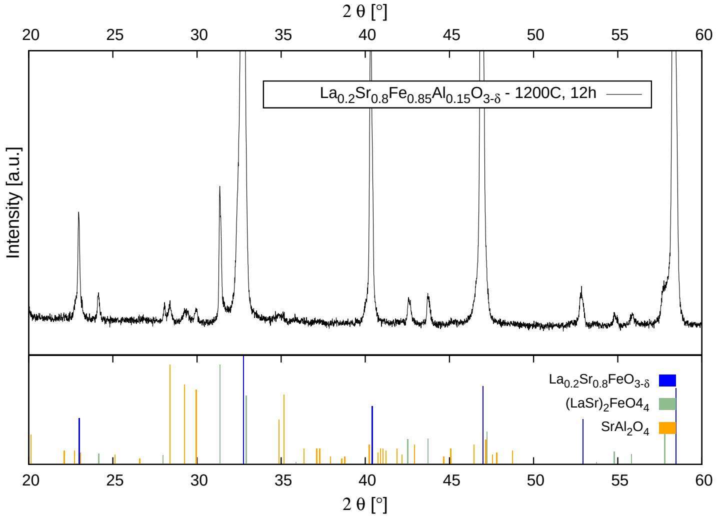

(b) XRD-pattern: $La_{0.2}Sr_{0.8}Fe_{0.85}Al_{0.15}O_{3\text{-}\delta}$

Figure 4.5: *XRD-patterns: Different compositions of LSFAl, note the different compositions in a) and b).*

As seen from Figure 4.5 the secondary phases ($SrAl_2O_4$ and $(LaSr)_2FeO_4$) were found for both tested compositions, however the composition with reduced strontium content showed less of the RD-phase after the first firing. Therefore the powder was crused, milled, and re-fired (blue xrd-pattern). After re-firing the powder showed less of both the RD and spinel phase.

Nano Alumina

Since it is widely known that the solid state reaction is kinetically slow and thus also a hindrance for high performance ceramic powder production the introduction of nano-sized alumina (Al_2O_3) was done. Nano-sized alumina should offer a higher reactivity during the calcination of the poweder, and the XRD-patterns for different firing temperatures can be seen in Figure 4.6.

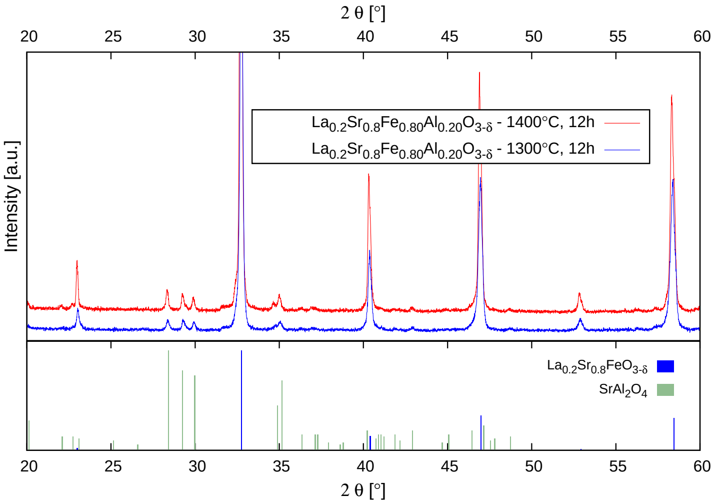

Figure 4.6: *XRD-pattern of LSFAl2882 made with nano-alumina*

It is seen that the RD-type phase is completely gone, and the only secondary phase present is the spinel phase ($SrAl_2O_4$). In addition to the LSFAl2882 composition a composition of the most promising composition ($La_{0.4}Sr_{0.6}Fe_{0.8}Al_{0.2}O_{3\text{-}\delta}$) from Figure 4.5 was prepared and fired at 1400°C.

4.1.3 Densification Behaviour

The densification behaviour of the coarse LSFAl2882 was determined by dilatometry, and the results can be seen in Figure 4.7. The green body and sintered densities were calculated by measuring the weight and dimensions of the sample before and after dilatometry and the results can be seen in Table 4.1.

Table 4.1: *Density of a coars LSFAl2882 green body before and after dilatometry*

	Pressing method	**% density of theoretical**
Greenbody	CIP (2000 bar)	64%
After DIL	-	84%

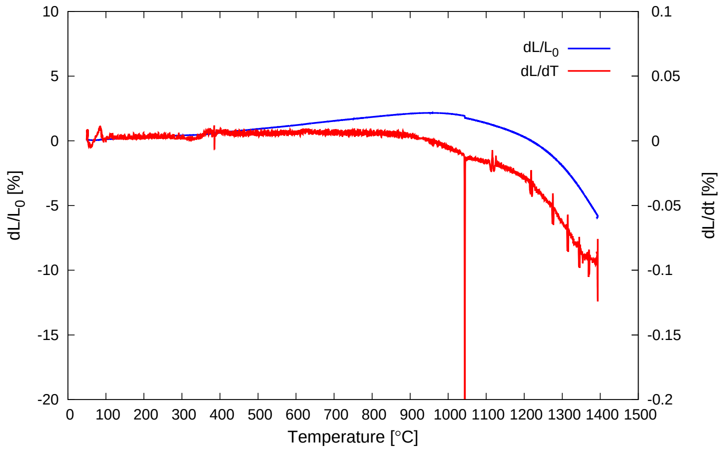

Figure 4.7: *Dilatometry curve for LSFAl2882*

4.1.4 Particle Size Distribution

The particle size distribution of the coarse LSFAl2882 powder prepared by the solid-state reaction can be seen in Figure 4.8.

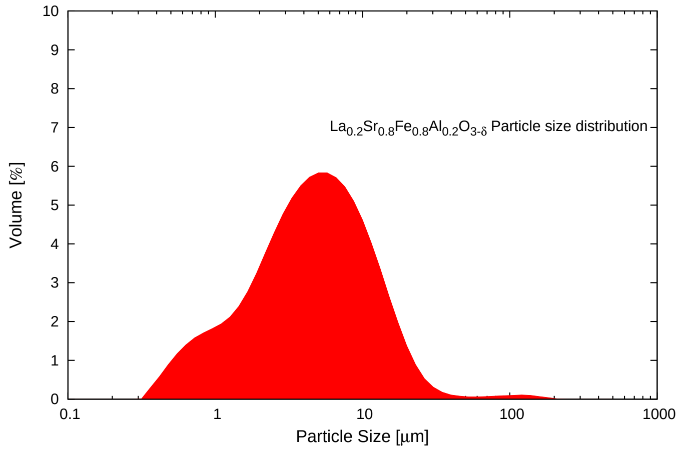

Figure 4.8: *Particle size distribution of coarse LSFAl produced by the solid-state reaction*

The distribution values (d) for the coarse powder are $d(0.10) = 0.9\mu m,\ d(0.5) = 4.3\mu m,\ d(0.9) = 12.5\mu m.$

4.1.5 Powder Surface Area

The course LSFAl powders surface area was measured by BET. The results from these measurements can be seen in Table 4.2

Table 4.2: *Powder surface area measured by nitrogen adsorption (BET)*

	Quantity	**Uncertainty**
BET Surface Area (1)	0.9704$[m^2/g]$	± 0.0006
BET Surface Area (2)	0.9744$[m^2/g]$	± 0.0025
Average BET Surface Area[3]	0.9706$[m^2/g]$	± 0.0006
BET particle size	1.12 $[\mu m]$	-

The particle size of the coarse LSFAl2882 powder was calculated from the BET surface area. This method assumes equi-sized spherical particles which is never the case, but allows for a relative good approximation. The complete as received data set from the BET measurements can be found in Appendix F.

---

[3] Average surface area calculated by a weighted mean. Formulas and calculations in Appendix E.

4.2 Porous Support Production

4.2.1 Phase Purity

The phase purity of the porous support after firing was measured by XRD and the results can be seen in Figure 4.9.

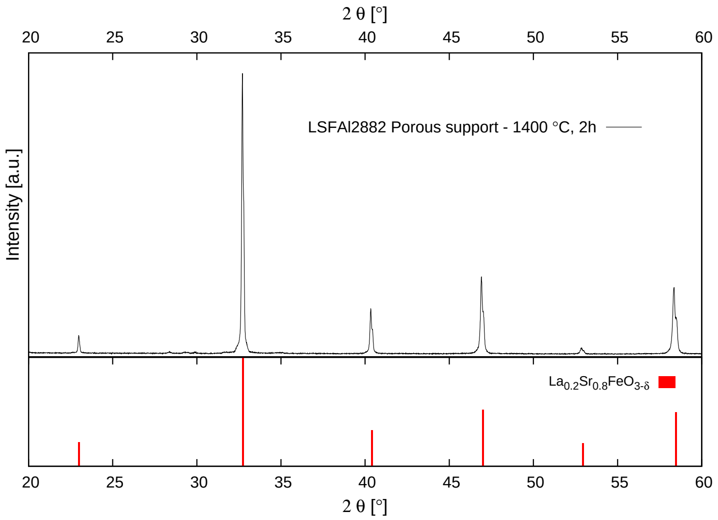

Figure 4.9: *XRD-pattern of the sintered LSFAl porous support (support was crushed for XRD measurement)*

There is still some trace of the $SrAl_2O_4$ phase in the porous support. However the amount seems to be insignificant when comparing the intensity of the named phase and that of the perovskite. As a comparison the XRD-pattern of the starting powder is included in the Figure 4.10 with the matched results from the diffractogram database, in addition the y-scale is logarithmic to further expose the secondary phases.

From Figure 4.10 it is seen that the Ruddlesden-Popper phase ($(LaSr)_2FeO_4$ is no longer present, however the spinel-phase ($SrAl_2O_4$) is still present.

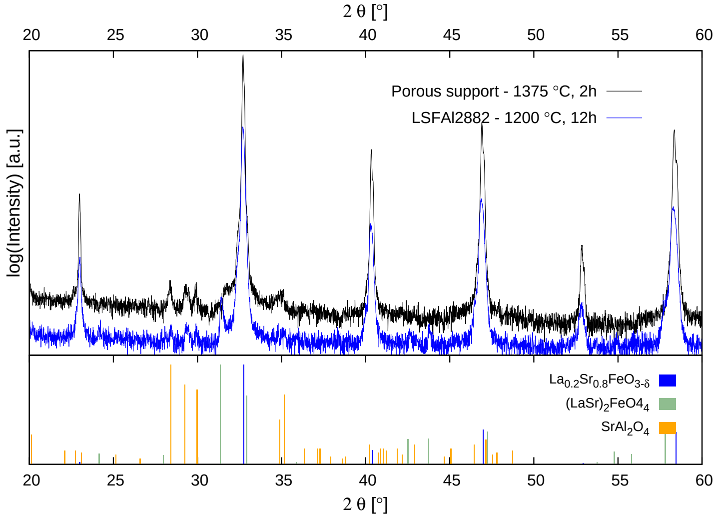

Figure 4.10: *XRD diagram of the calcined LSFAl powder and powder from the porous support (crushed after firing). Note the logaritmic y-axis*

4.2.2 Morphology

The morphology of the prepared porous supports was studied by SEM and micrographs are presented in Figure 4.11.

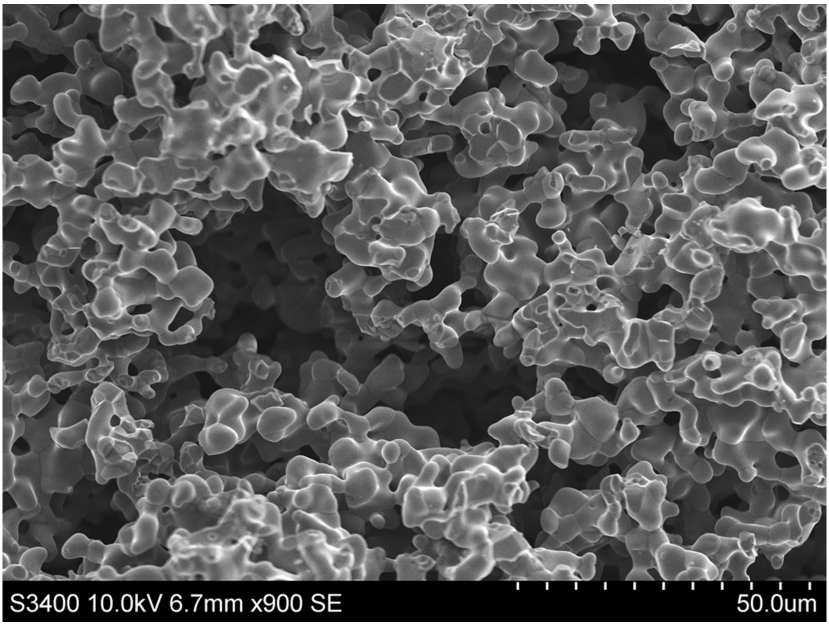

(a) Cross section of porous support

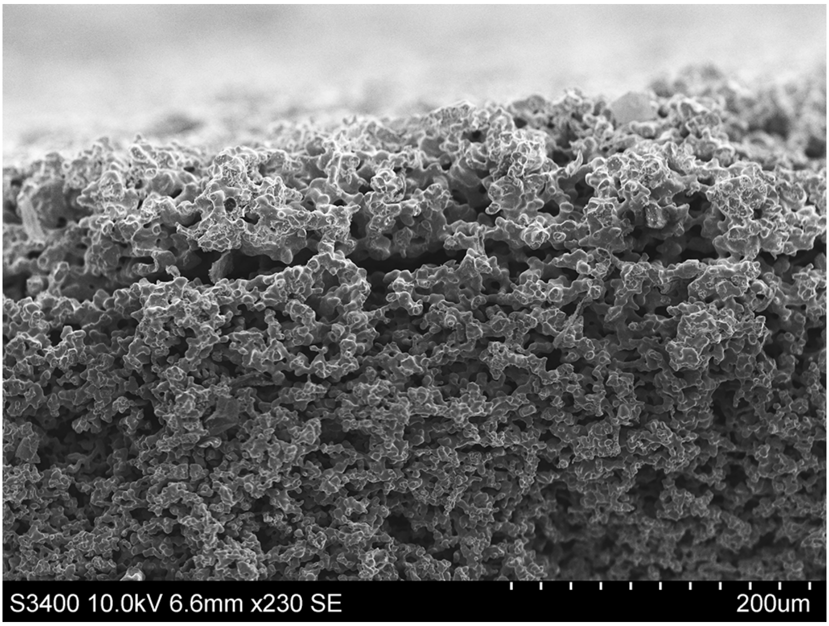

(b) Cross section of porous support

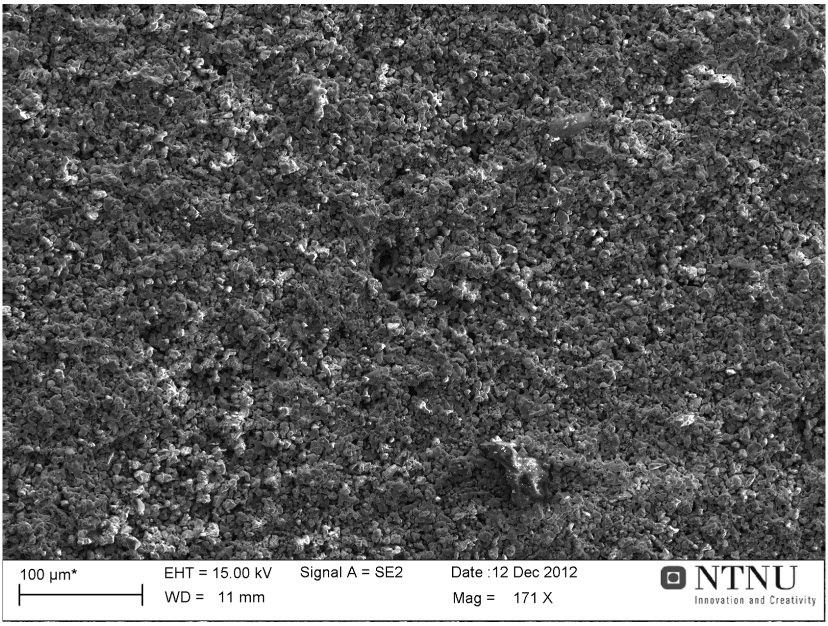

(c) Top surface of the porous support

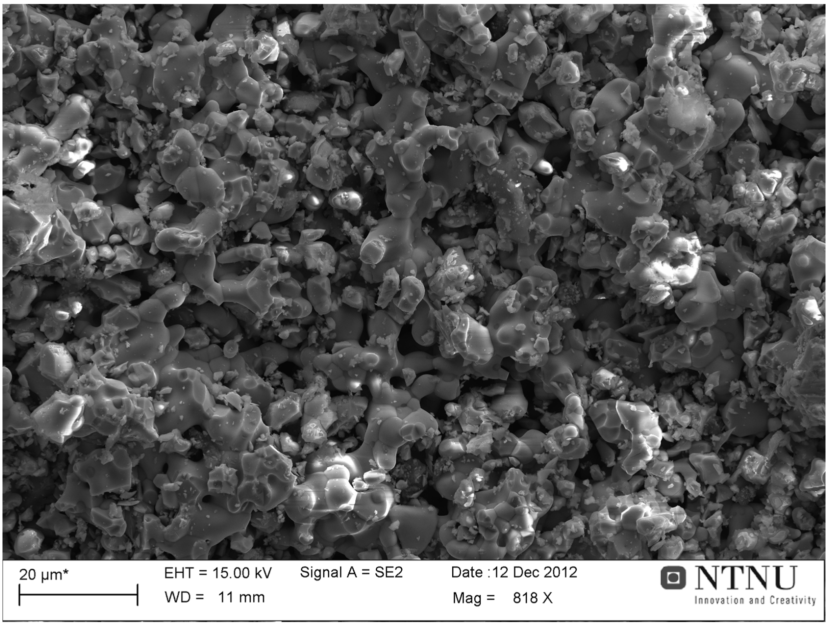

(d) Top surface of the porous support, note the different scale

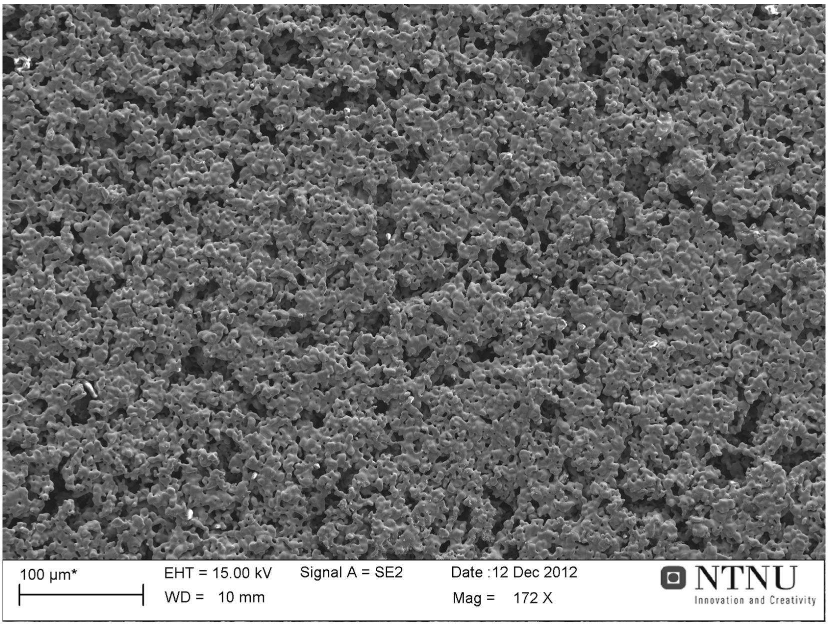

(e) Bottom surface of the porous support

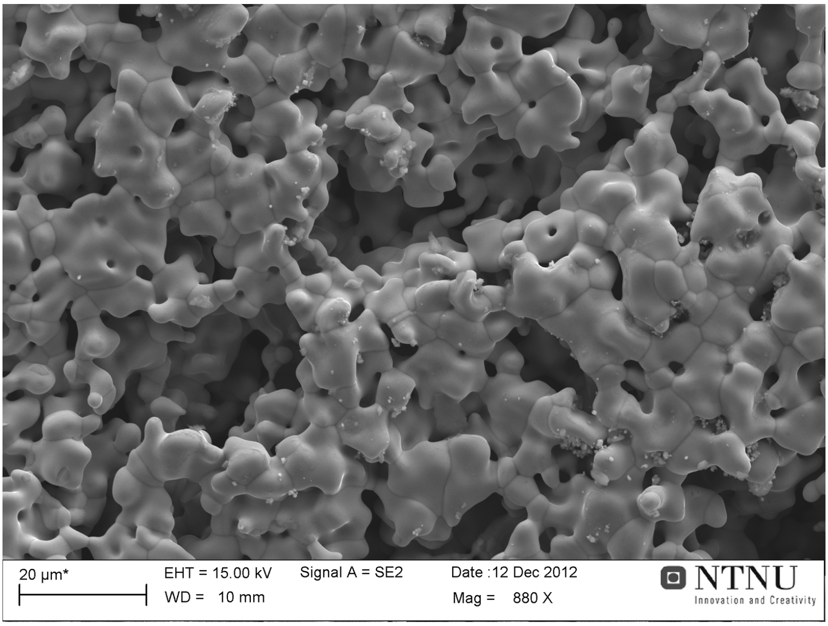

(f) Bottom surface of the porous support, note the different scale

Figure 4.11: *SEM micrographs of porous support, a)-b) Cross sections, c)-d) top surface, and e)-f) bottom surface*

4.2.3 Porosity

The porosity of some random small samples of the produced porous supports was measured according to the ISO-5017:1998 standard, and the results can be seen in Table 4.3.

Table 4.3: *True porosity of porous supports*

Sample	m_1	m_2	m_3	π_t
# 1	0.1032	0.0881	0.1256	61.2%
# 2	0.0972	0.0830	0.1185	61.4%
Average	-	-	-	61.3%

4.2.4 Gas Permeability of Porous Support

The gas permeability of the porous support was measured, and the Knudsen permeability coefficient (K_0) and the specific permeability coefficient (B_0) was determined by plotting $K(293K)$ vs. $\bar{p}$. The plot can be seen in Figure 4.12.

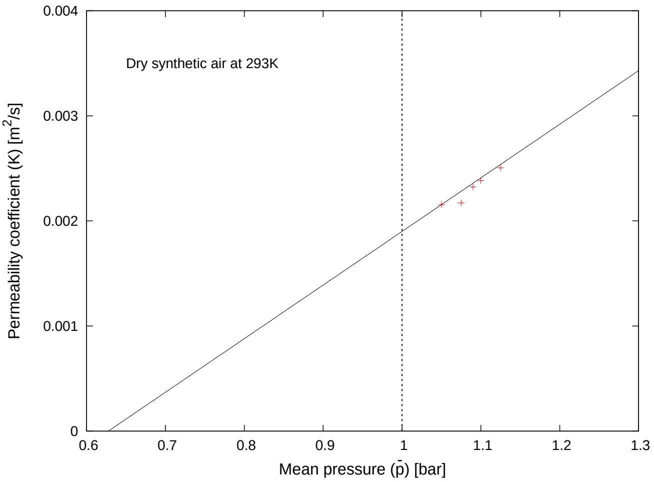

Figure 4.12: *Permeability coefficient of a porous support*

Since the experimentally determined Knudsen permeability coefficient is less than zero ($K_0 = -0.0032$) viscous flow is assumed to be the only mechanism contributing to the gas flow through the porous support, and the gas permeability was calculated by using Equation 2.16. The permeability of the porous support is presented both in Figure 4.13 and summarized with other permeation and porous support parameters in Table 4.4.

Table 4.4: *Summary of permeation- and porous support parameters*

Constant	Value	Uncertainty	Unit
K_0	-0.0032	-	$m^2 s^{-1}$
$B_0(calc.)^4$	$4.36 \cdot 10^{-8}$	$1.23 \cdot 10^{-}9$	m^2
$B_0(slope)^4$	$1.05 \cdot 10^{-7}$	-	m^2
D	3.95	0.23	nPm
r^5	60	1	μm
$Kn(300K, 1bar)^5$	$1.2 \cdot 10^{-3}$	-	-

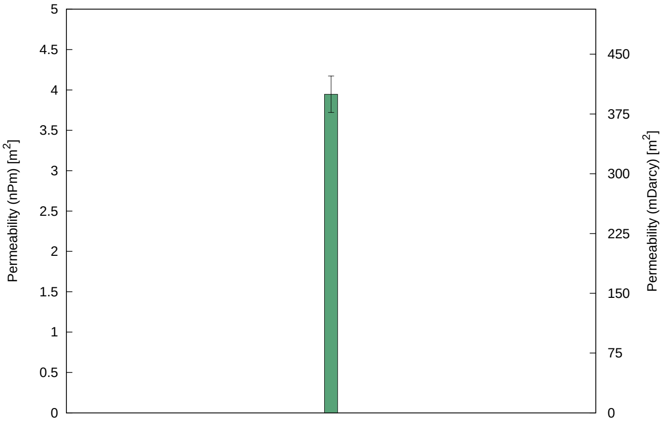

Figure 4.13: *Gas permeability of a porous support*

A theoretical calculation of the gas permeability at elevated temperatures for different pressure drops across the porous support was done, and the results can be seen in Figure 4.14[6]. The low pressure drops used in the calculation is because the porous support is intended to support a dense thin film. When a dense thin film is attached to the porous support the pressure drop across

---

[4] The calculated B_0 value is from rearranging Eq. 2.14 and assuming $K_0 = 0$, whereas the value from the slope is calculated with the K_0 value from the linear regression ($K_0 = -0.0032$).

[5] The throat pore radius, r, is calculated from Eq. 2.20, and the Knudsen number, Kn, is calculated from Eq. 2.17

the support itself is assumed to be low. In addition the Knudsen number for elevated temperatures was calculated and the results is presented in Figure 4.15

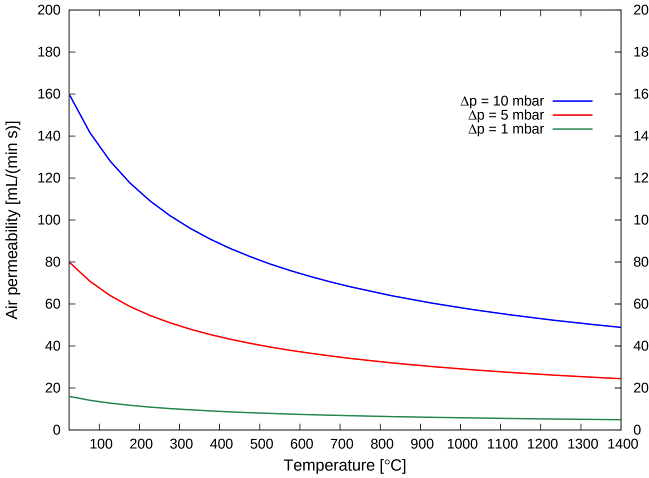

Figure 4.14: *Expected gas permeation of the porous support at elevated temperatures for different pressure drops.*

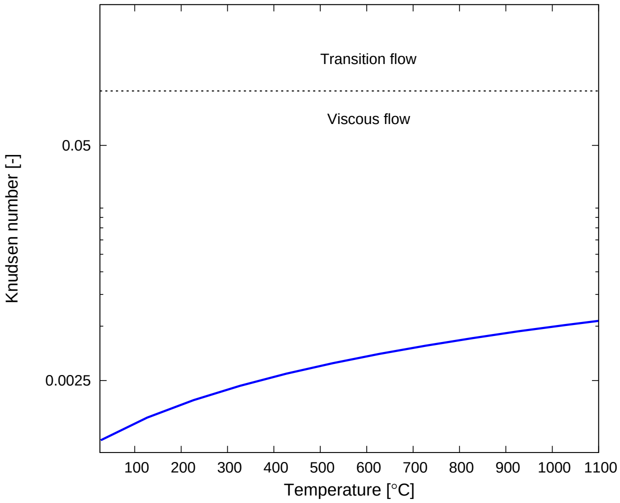

Figure 4.15: *Evolution of the Knudsen number with temperature, pressure held constant at* $\overline{p} = 1.005\text{bar}$.

---

[6] Eq. 2.16 was used to calculate the gas permeability at different temperatures (with *D*-value given in Table 4.4). Viscosity values used for calculation are from Kadoya et. al. [34].

4.3 Asymmetric Membrane Production

The green body produced by tape casting was dip-coated according to Section 3.2.3. Gas tight asymmetric membranes was not successfully produced in this work, as shown in Figure 4.17, however progress was made from the first membrane made to the last, as shown in Figure 4.19.

4.3.1 Phase Purity

The phase purity of the dense functional layer of the asymmetric membrane presented in Figure 4.17 was studied by XRD, and the result is presented in Figure 4.16.

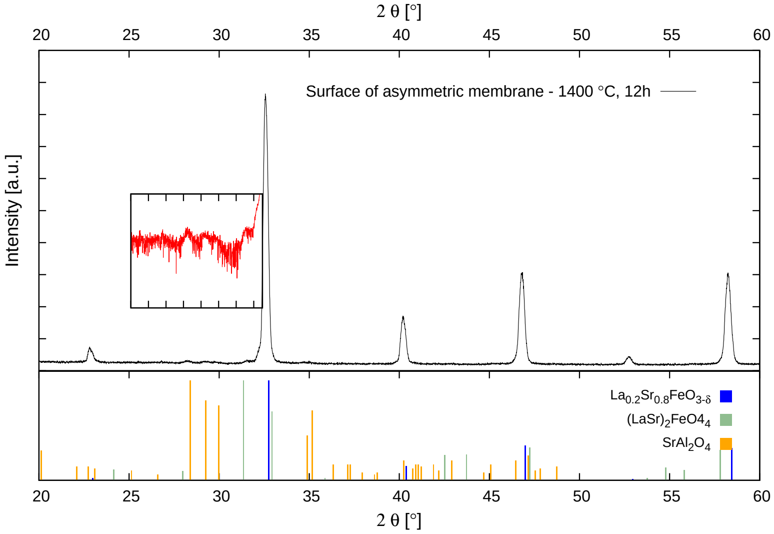

Figure 4.16: *XRD-pattern of the sintered asymmetric membrane. The XRD measurement was done on the surface of the dense functional layer. Note the highlighted region (in red) exposing the presence of* $SrAl_2O_4$.

As seen there are traces of the same secondary phase on the surface of the asymmetric membrane as seen both in the prepared coarse LSFAl2882 powder (Fig. 4.3(a)-(b)) and the porous support (Fig. 4.9).

4.3.2 Morphology

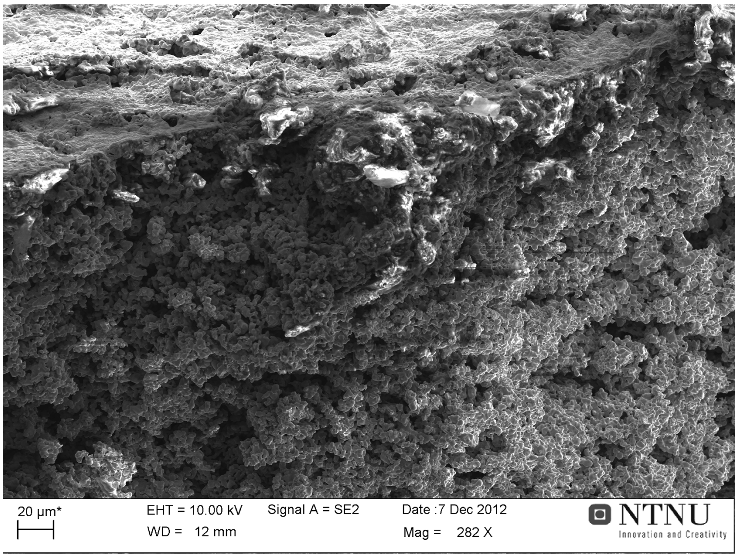

(a) Cross section of the asymmetric membrane

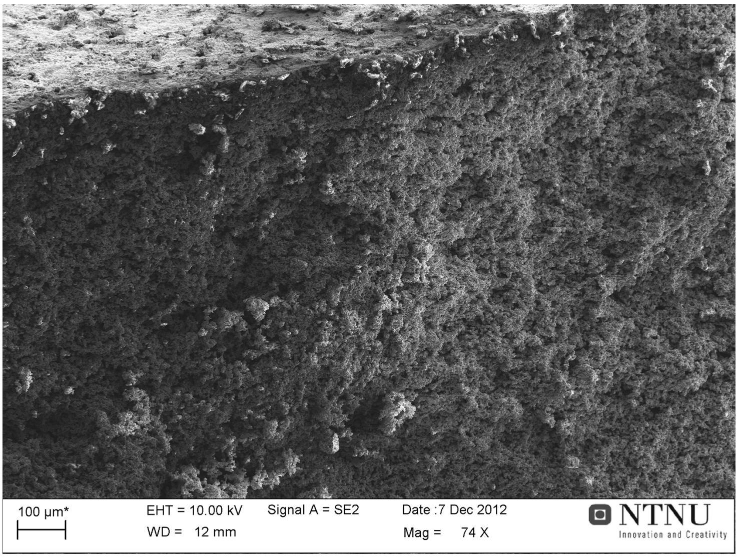

(b) Cross section of the asymmetric membrane

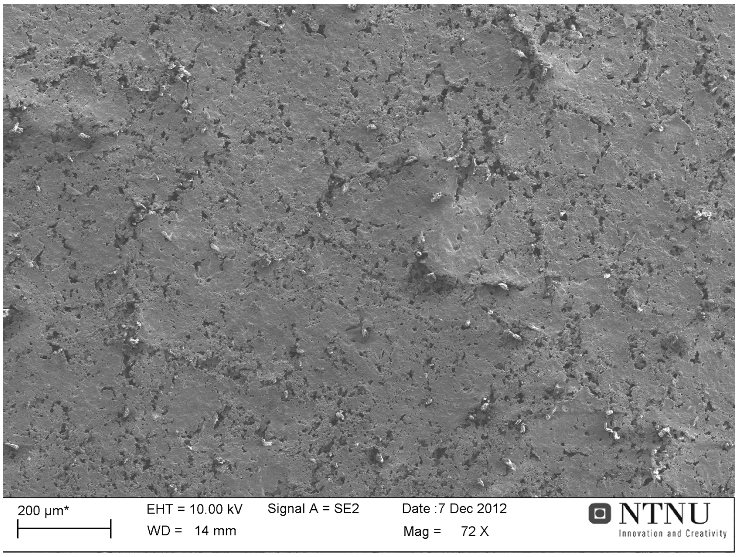

(c) Dense layer surface: overview

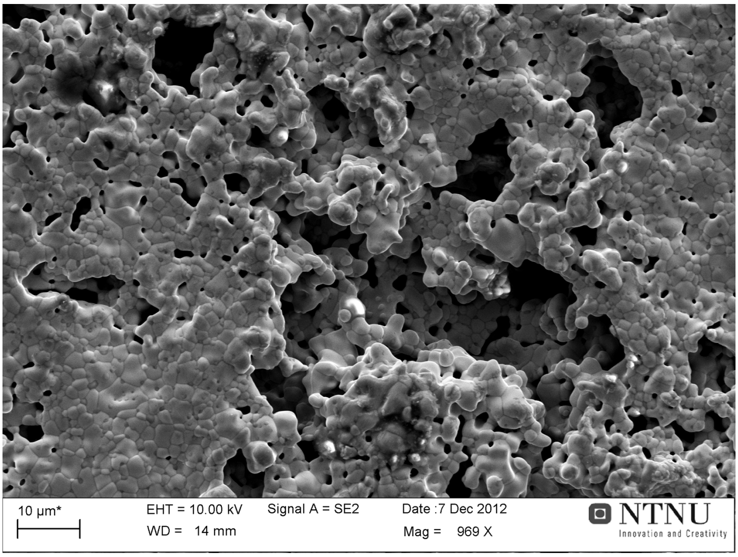

(d) Dense layer surface: cracks

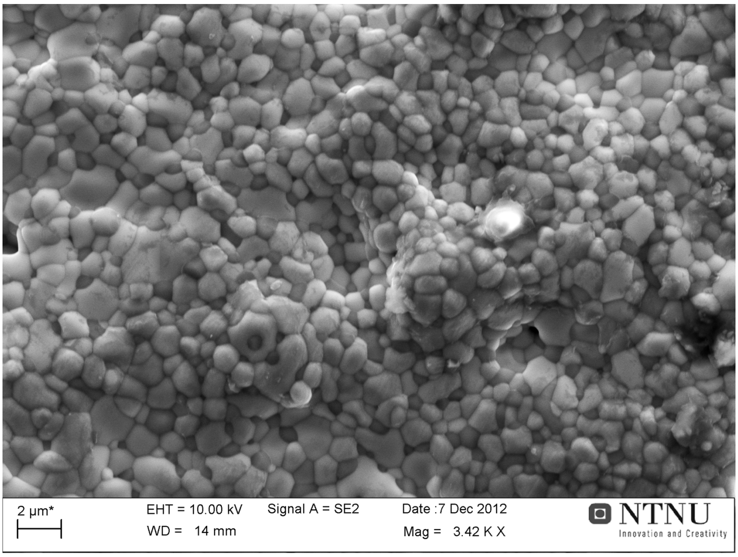

(e) Dense layer surface: dense part

Figure 4.17: *SEM micrographs of the produced asymmetric membrane, a)-b) Cross sections, c)-e) dense layer surface (different magnifications)*

SEM micrographs was also taken by utilizing the backscatter detector to identify any secondary phases on the surface of the dense functional layer. The results can be seen in Figure 4.18

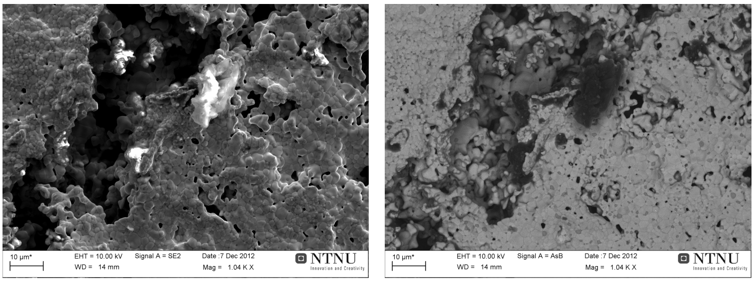

(a) Dense layer surface: SE2-detector **(b)** Dense layer surface: AsB-detector

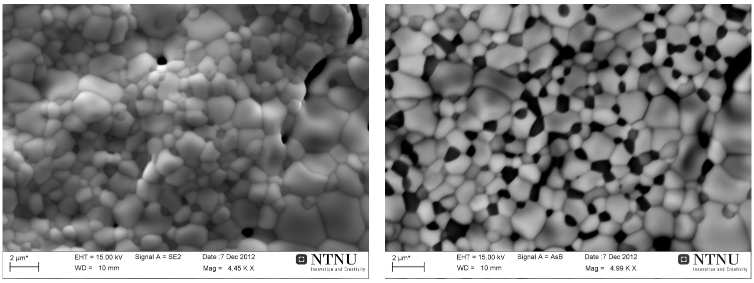

(c) Dense layer surface: SE2-detector

(d) Dense layer surface: AsB-detector

Figure 4.18: *SEM micrographs: comparing micrographs taken with the secondary electron detector and the backscatter detector*

Since the dense top layer contained secondary phases an EDS-analysis was done on the surface. The points for the analysis were taken from one light and dark region in the micrograph presented in Figure 4.18(d), and the EDS-spectra is presented in Appendix G.

A comparison between the first membrane and the last membrane made can be seen in Figure 4.19. The difference between the two membranes are the number of dip-coated layers applied after the first firing.

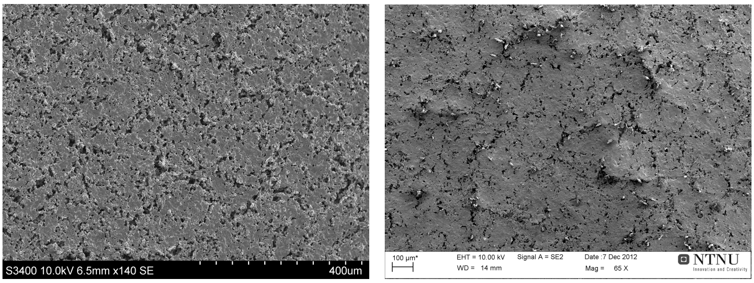

(a) Asymmetric membrane (dip-coated 1 time after first firing)

(b) Asymmetric membrane (dip-coated 3 times after first firing)

Figure 4.19: *SEM micrographs: comparing micrographs of two asymmetric membranes*

Chapter 5

Discussion

5.1 LSFAl Powder Synthesis

As seen from Figure 4.3(a)-(b) there are at least two secondary phases present in the calcined powder. These phases were identified by matching the undistinctive LSF XRD-peaks with the best results from the ICCD's PDF4+ database. The best match of came from $SrAl_2O_4$ and $(LaSr)_2FeO_4$. When looking at the following general relation, Viz.:

$$3ABO_3 \quad \longleftrightarrow \quad A_2BO_4 + AB_2O_4 + \frac{1}{2}O_2 \tag{5.1}$$

the observed phases seems plausible and it is also reported in literature that $SrAl_2O_4$ is known to precipitate out from e.g. $SrFe_{1\text{-}x}Al_xO_{3\text{-}\delta}$ (SFAl) [14, 18]. Previous work done by Wagner, N. showed what seems to be phase pure LSFAl2882 powder [7]. However, there is a significant difference in the powder production method. The powder in this work was prepared by the solid state reaction (SSR), whereas the powder used by Wagner was prepared by spray pyrolysis. Spray pyrolysis offers close to an atomic-to-atomic homogeneous reaction between the precursors. This means increased reaction kinetics compared to SSR, which could play a part in hindering the formation of secondary phases. Furthermore, it is also reported in literature that $SrFe_{1\text{-}x}Al_xO_{3\text{-}\delta}$ (SFAl) was produced phase pure with the glycerol-nitrate method for: $0 \leq x \leq 0.3$. The glycerol-nitrate method is more similar to spray pyrolysis than to SSR, which seems to further support the argument of reaction kinetics and particle size.

Phase pure LSFAl2882 was not prepared by the solid state reaction in this work. Reasons for this might be slow reaction kinetics due to large precursor particles. The precursors used during powder preparation had particle size in the micrometer scale, and the kinetics of the reaction could be the reason for the i.e. slow incorporation of Al_2O_3 into the LSF lattice. This seems plausible when the spray pyrolised powder used by Wagner was reported to be phase pure. Therefore LSFAl2882 was also prepared by using nano-alumina powder ($\varnothing < 60$ nm). The XRD-pattern (Figure 4.6) of LSFAl2882 powder samples prepared with nano-alumina shows that the Ruddlesden-Popper (RD) type phase $(LaSr)_2FeO_4$ is gone, however the spinel phase $SrAl_2O_4$ is still present. Since the thermodynamic stability of this phase ($SrAl_2O_4$) compared to the perovskite (LSFAl) is not known it could be that the formation of the spinel phase is favoured. This could also explain why there is substantially more of the spinel in the powder prepared with nano-alumina as a precursor. After formation of the spinel phase it can be seen from the phase diagram of the $SrO-Al_2O_4$-system (Figure 2.4) that the phase is stable until relative high temperatures (T=1760°C). This, in addition to the unknown thermodynamically stability of the phase, is probably why the secondary phase remains in the powder when the firing temperature was increased. This applies both to the powder where nano-alumina and micro-alumina was used as a precursor. The RD-phase diminishes with increased firing temperature, which is expected, and there is no trance of it in the XRD-pattern taken of the porous support which was fired at 1400°C. The relative amount of the spinel phase was determined using the software *Topas* and the amount of the spinel phase in different stages of the asymmetric membrane production can be seen in Table 5.1.

Table 5.1: *Amount of the secondary $SrAl_2O_4$-phase in different*

	wt% $SrAl_2O_4$[1]
Coarse LSFAl2882	2.04
Porous support	3.46
Surface asymmetric membrane	5.92
Nano-alumina LSFAl2882	12.6

The presence of secondary phases will change the composition of the intended perovskite (LSFAl2882), and for the powder prepared with nano-alumina all of the Al^{3+}-cations are found in the secondary phase, thus shifting the original LSFAl2882 composition to a LSF perovskite. When removing all of the Al^{3+} from the perovskite there is a surplus of either La^{3+}- or Sr^{2+}-cations ($La_xSr_y > 1$) and it would be expected to find additional secondary phases such as SrO or La_2O_3. However, there could not be determined any other secondary phases from the XRD-patterns obtained during this work. A reason for this could be that the amount these expected phases are so small compared to the detected phases that the XRD-signal blends inn with the background noise. From the *Topas*

---

[1] Amount of secondary phase determined with the software *Topas* using cubic ($Pm\bar{3}m$) $La_{0.2}Sr_{0.8}FO_3$ and monoclinic (P21) $SrAl_2O_4$ unit cell, complete analysis data given in Appendix H

analysis the best fit of the XRD-patterns for the porous support, asymmetric membrane, and the powder prepared with nano-alumina came from using the unit cell of the rombohedral ($R\overline{3}c$) $La_{0.4}Sr_{0.6}FeO_{3-\delta}$ perovskite, as seen in Figure H.1(b)-(g). It is reported that the LSF perovskite will shift from cubic ($Pm\overline{3}m$) to rombohedral ($R\overline{3}c$) when the Sr^{2+}-content decreases, this is illustrated in the pseudo-binary phase diagram presented by Fossdal et. al. [13] (Figure 2.2). Due to the best overall match when using the rombohedral unit cell it is reasonable to assume that when the Al^{3+} content decreases the perovskite system compensates by incorporating less Sr^{2+}, and thus one would expect to see some traces of SrO.

Since phase pure LSFAl2882 was not prepared in this work, a short study of different LSFAl compositions were done to see if change the $A_{1(1\text{-}x)}A_{2(x)}$ and $B_{1(1\text{-}x)}B_{2(x)}$ cation ratio would yield a phase pure powder. $La_{0.4}Sr_{0.6}Fe_{0.8}Al_{0.2}O_{3-\delta}$, and $La_{0.2}Sr_{0.8}Fe_{0.85}Al_{0.15}O_{3-\delta}$ were produced, and from the results of this short study, which can be seen in Figure 4.5, $La_{0.4}Sr_{0.6}Fe_{0.8}Al_{0.2}O_{3-\delta}$ showed promising results after the second firing. However, it was decided to produce the porous support with LSFAl powder of the same composition as the thin dense functional layer (LSFAl2882).

Sintering and Densification Behaviour

The sintering behaviour of the coarse LSFAl2882 powder was investigated by dilatometry upto 1400°C, and as seen from Figure 4.7 the sample did not reach the maximum contraction rate (optimal sintering temperature), but from the dilatometry curve it is estimated that the optimal temperature is around 1450°C. Before the dilatometry measurement the green body density was calculated to 64% of theoretical density. After the experiment the calculated density of the sample was 84% of theoretical density. The low sample density can be due to e.g. too low temperature, slow reaction kinetics, no dwell time at maximum temperature, or most likely because the particle size of the coarse powder is quite large. There was no attempt to try higher temperatures when the melting point of LSFAl2882 is not known. The prepared LSFAl2882 powder was only used to produce the porous support, and since that support should be as porous as possible the densification during sintering is not as important as for the dense functional layer. The porous support only needs enough densification to produce neck growth between particles, so that it gains enough mechanical strength to support the dense functional layer during operation.

Particle Size and Surface Area

The particle size distribution was adjusted by planetary milling until a desirable distribution in the low µm range was reached. The large particle sizes seen in Figure 4.8 was believed to be agglomerates, which was confirmed by SEM. Since the particles have a quite large size the surface area was expected to be low. The measured surface area by BET confirmed this, and the coarse LSFAl2882 powder had a surface area of $0.9706[m^2/g]$ $\pm 0.0006[m^2/g]$.

5.2 Porous Support Production

Tape casting was the method used for porous support production in this work. Tape casting requires that the LSFAl2882 powder and pore former (carbon black) is suspended in a slip. The slip needs to have a low viscosity, but not so low that it does not flow. The slip used in this work (described in Table 3.6) produced a viable tape, however the reproduction potential is considered low. Two of three tapes were usable, but one of the casted tapes showed some rather strange properties. During the final slow rolling the slip agglomerated which in turn resulted in a unusable slip. The reasons for this is not known, but it is suspected it can either be because of an old binder solution (PVA) or because of the addition of the commercial chemical BYK-3455, whose content is not know. Due to time limitations this was not further investigated.

The prepared tape had a LSFAl2882 content of 60 vol% and a carbon black content of 40 vol%, and was approximately 300 µm thick after drying. After a test firing according to the temperature program shown in Figure 3.5 the number of laminates needed to make an approximately 1 mm thick support was determined to be 6. The measured porosity after firing was determined by the Archimedes method to be 62.3 %. This measured porosity seems high when comparing it with values done in previous work. However the SEM micrographs of the porous support (Figure 4.11(a)-(b)) shows a very high connected porosity. Therefore the measured porosity by the Archimedes method seems plausible, and is considered valid.

Phase Purity

After firing the phase purity of the porous support was studied by XRD. The support was mortared down into powder before the XRD-analysis. The XRD-pattern shows that the RD-type phase has deminished and is not detected, however the $SrAl_2O_4$ spinel phase is still present (Figure 4.9), the relative amount of the spinel phase compared to the perovskite was estimated with the software *Topas*, and the result can be seen in Table 5.1. When comparing the powder before and after porous support production there has been an increase of the unwanted spinel phase, however the amount is small and it is not known if the difference between the two powders (coarse LSFAl2882 and crushed porous support) is less than the uncertainty of the measurement. No further effort was done to clarify or investigate the reasons of the presence of the secondary phase.

Gas permeability

The gas permeability, D, of the porous support was calculated from the results presented in Figure 4.12 and was determined to be $D = 3.95\ nPm \pm 0.23\ nPm$. The gas permeability can be described by the following equation (Eq. 2.14 + 2.15):

$$J(T,p) = \left(K_0(T) + \frac{B_0}{\eta(T)} \overline{p} \right) \frac{\Delta p}{l}$$

where K_0 is the Knudsen permeability coefficient and B_0 is the geometric factor of the porous material. The Knudsen permeability coefficient must be greater than or equal to zero ($K_0 \geq 0$), but from the linear regression of the collected results presented in this work $K_0 = -0.0032$. This is believed to be because of uncertainty connected to the experimental setup. The calculations done are very pressure sensitive, and the pressure gauge used to measure the overpressure during the experiment was not considered to be of high precision. It was also hard to determine the uncertainty of the pressure gauge and this was not done. If the Knudsen permeability coefficient is zero that means that the gas flow through the porous material is completely govern by viscous flow, and thus is only pressure, temperature, and gas viscosity dependant. The throat pore radius (r) was calculated, and the results gave a radius of $r = 60$ µm ± 1 µ. This value is very large when comparing to SEM micrographs of the porous support, however there seems to be a lot of connected porosity which could explain the large calculated value of the throat pore radius. The throat pore radius was used to calculate the Knudsen number (Kn) over a large temperature range and the results were presented in Figure 4.15. The mean free path of the gas was calculated at each temperature interval, and this is the reason for the increasing Knudsen number with increasing temperature. The Knudsen number at high temperatures is low, and when comparing it to the critical value reported by Ziarani et. al. it is well below the critical value even at elevated temperatures ($Kn << 0.1$) [29]. The gas permeability performance of the porous support at elevated temperatures was simulated using Equation 2.16, and the results was presented in Figure 4.14. Some summarized data can be seen in Table 5.2.

Table 5.2: *Expected permation at elevated temperatures*

Δp	**Temperature** [$°C$]	**Air permeation [mL·min^{-1}·cm^{-2}]**
1 mbar	800	6.4
	900	6.0
	1000	5.8
5 mbar	800	32
	900	30
	1000	29
10 mbar	800	64
	900	60
	1000	58

From these results it is seen that even at relative low pressure drops across the porous support the performance at high temperatures should be enough to not limiting the rate of the oxygen separation flux through the dense functional layer. The permeation values obtained in this work were compared to values reported by Wagner, N. the support material is the same (LSFAl2882), however the production method is different. In this work the porous support was produced by tape casting, Wagner produced the porous support by uniaxial pressing.

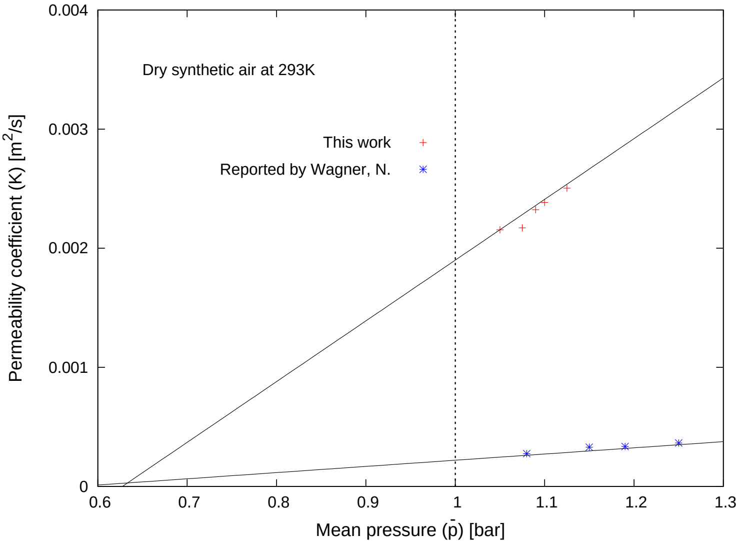

Figure 5.1: *Comparison of the gas permeability of a porous support produced by tape casting (this work) and by uniaxial pressing (Wagner, N. [7])*

When taking into consideration the results reported by Wagner (6.5 times lower porous support gas permeation), and when looking at the high oxygen separation fluxes reported for the asymmetric membrane in the same work (15 mL·min^{-1}·cm^{-2}, 1000°C, $\log(p_{O_2}/atm) = -1.5$) [7] the performance of the porous support produced in this work should be satisfactory.

5.3 Asymmetric Membrane Production

No viable asymmetric membrane was produced during this work, however progress towards producing a gas tight asymmetric membrane was made. The deposition technique for applying the dense functional layer was dip-coating, and the dip-coating solution was prepared from spray pyrolysed LSFAl2882 powder. The spray pyrolysed powder has a much smaller particle size compared to the coarse LSFAl powder used in this work. This gives rise to at least two problems which could be the cause for cracking seen in the dense functional layer.

1. The pore size of the porous support is too large compared to the particle size of the particles in the dip-coating solution. This would mean that the particles that should make up the dense layer falls into the porous support.
2. Since the dense layer is made up from nano sized particles it will shrink considerably more than the porous support during firing, thus creating cracks in the surface.

From the SEM micrographs presented it seems like shrinking during firing is the main problem, however one cannot exclude the possibility that also particles falls into the large pores of the porous support when the binder etc. burns off during the first firing. The porous support green body was dip-coated once, fired at 1100°C, then dip-coated one/three times and fired again at 1400°C. The difference between the two membranes are small but noticeable, and the membrane which was dip-coated the most times seems to shows less large cracking and larger areas which have completely densified.

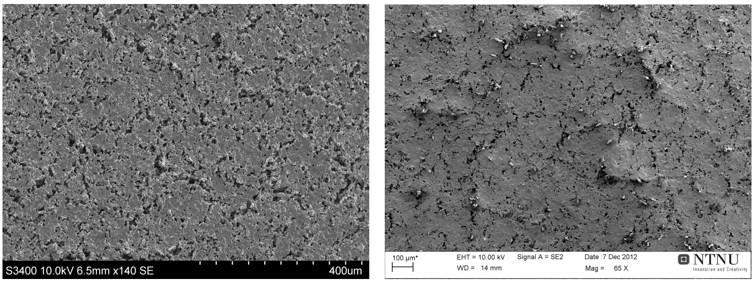

(a) Asymmetric membrane (dip-coated 1 time after first firing)

(b) Asymmetric membrane (dip-coated 3 times after first firing)

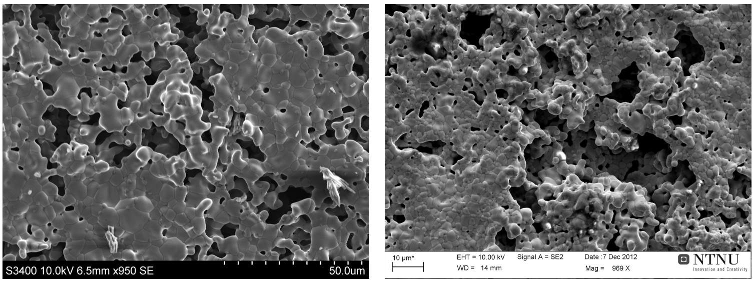

(c) Asymmetric membrane (dip-coated 1 time after first firing)

(d) Asymmetric membrane (dip-coated 3 times after first firing)

Figure 5.2: *SEM micrographs: comparing micrographs of two asymmetric membranes, dip-coated one and three times after the first firing*

However the thickness of the dense layer in both cases is very low, and from the figure below it is seen that the thickness is only in the low µm-range for both of the membranes, when in previous work the thickness of the dense layer was in the range $10 \leq \mu m \leq 20$ for the same amount of depositions [3, 6, 7, 22].

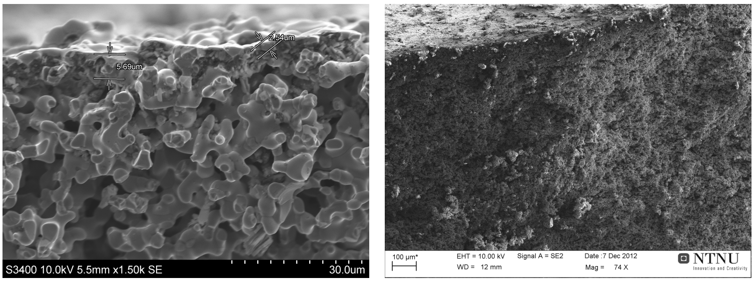

(a) Asymmetric membrane (dip-coated 1 time after first firing)

(b) Asymmetric membrane (dip-coated 3 times after first firing)

Figure 5.3: *SEM micrographs: comparing micrographs of two asymmetric membranes*

From these results the most viable membrane is considered to be the one dip-coated three times after the first firing, however more work needs to be done to optimize the deposition technique on a substrate with such large pores.

Phase Purity

The XRD-pattern of the dense layer's surface shows traces of the same secondary $SrAl_2O_4$ phase as seen throughout this work (Fig 4.16). The surface was examined by SEM and the secondary phase is clearly visible from the micrograph recorded with the electron backscatter detector.

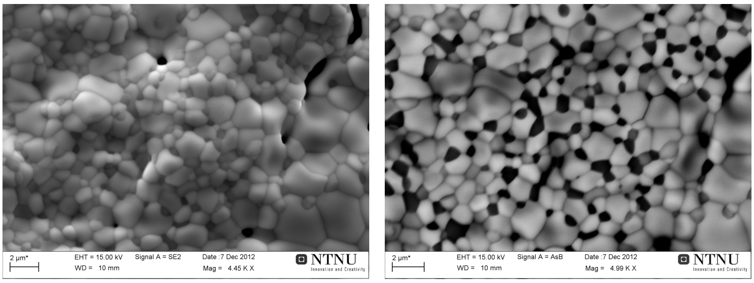

(a) Dense layer surface: SE2-detector **(b)** Dense layer surface: AsB-detector

Figure 5.4: *SEM micrographs: comparing micrographs taken with the secondary electron detector and the backscatter detector*

A EDS-analysis of the bright and dark grains seen in Figure 5.4(b) was done. From the recorded EDS-spectra (Fig. G.1) it is seen that the Al content in the secondary phase is much higher than for the main phase. This is in accordance with the XRD-analysis which matched the secondary phase to the spinel $SrAl_2O_4$.

Throughout this work the presence of the $SrAl_2O_4$ phase has been evident, and effort to reduce and/or remove this phase from the coarse LSFAl2882 powder has proven to yield no result. Due to time restraints no effort was done to look into the thermodynamics of LSFAl2882 and $SrAl_2O_4$. If the Gibbs free energy speaks in favour for the formation of the spinel compared to the perovskite the production of phase pure LSFAl2882 by the solid state reaction method would be difficult.

Air permeability

Since no viable asymmetric membrane was produced during this work no air permeation measurements could be done. However, if a asymmetric membrane could be made gas tight with the porous support produced in this work the air permeation is expected to at least be in the same region as reported by Wagner, N.

Chapter 6

Concluding Remarks and Further Work

- Coarse $La_{0.2}Sr_{0.8}Fe_{0.8}Al_{0.2}O_{3-\delta}$ (LSFAl2882) was prepared by the solid state reaction. The prepared powder was not phase pure, and there were traces of $SrAl_2O_4$ and $(LaSr)_2FeO_4$.

- A short phase study of LSFAl was done to try and make a phase pure powder. The compositions $La_{0.2}Sr_{0.8}Fe_{0.8}Al_{0.2}O_{3-\delta}$, $La_{0.4}Sr_{0.6}Fe_{0.8}Al_{0.2}O_{3-\delta}$, and $La_{0.2}Sr_{0.8}Fe_{0.85}Al_{0.15}O_{3-\delta}$ were synthesised by the solid state reaction. And from the obtained results LSFAl4682 was the most promising composition with respect to phase purity. Additionally $La_{0.2}Sr_{0.8}Fe_{0.8}Al_{0.2}O_{3-\delta}$ was prepared using nano-alumina powder as a precursor, and the XRD-results showed that all of Al was found in the secondary $SrAl_2O_4$ phase.

- Porous supports were made from the coarse LSFAl2882 powder. Carbon black was used as a pore former and the green body was produced by tape casting. After firing at 1400°C the porosity was determined by Archimedes method to be 62.3 %. There was no trace of the $(LaSr)_2FeO_4$ secondary phase in the porous support, however the $SrAl_2O_4$ secondary phase was still present. The gas permeability of the porous support was determined at room temperature, and estimates of the permeability at elevated temperatures and different pressure drops across the support were done. The gas permeability at 1000°C and a pressure drop of $\Delta p = 10$mbar was calculated to be 58 $mL \cdot min^{-1} \cdot cm^{-2}$. Furthermore the throat pore radius, r, was calculated from the permeability data which in turn was used to calculate the Knudsen number over a wide temperature range. Even for high temperatures ($T > 1000$°C) the Knudsen number of the porous support is well below the critical value for viscous flow.

- Asymmetric membranes were prepared by dip-coating the green body produced by tape casting. After dip-coating the green body was calcined at a intermediate temperature of 1100°C. The intermediate asymmetric membrane was dip-coated again and fired at 1400°C to increase the probability of producing a gas tight membrane. No gas tight asymmetric membranes were produced during this work.

The presence of the secondary $SrAl_2O_4$ phase throughout all the different stages during this work rises questions about the stability of LSFAl2882. Further work could include a study to determine thermodynamical properties of LSFAl2882.

The high porosity of the produced porous support is promising, and further work should include optimization of the way the thin dense functional layer is deposited onto the tape casted green body, which could result in a gas tight asymmetric membrane.

No mechanical testing of the porous supports was done during this work due to time restraints, therefore further work should include mechanical testing of the porous support.

Bibliography

[1] H.J.M. Bouwmeester. Dense ceramic membranes for methane conversion. *Catalysis Today*, 82(1-4):141–150, July 2003.

[2] P.V. Hendriksen, P.H. Larsen, M. Mogensen, F.W. Poulsen, and K. Wiik. Prospects and problems of dense oxygen permeable membranes. *Catalysis Today*, 56(1-3):283–295, February 2000.

[3] J. Gurauskis, Ø.F. Lohne, H.L. Lein, and K. Wiik. Processing of thin film ceramic membranes for oxygen separation. *Journal of the European Ceramic Society*, 32(3):649 – 655, 2012.

[4] J. Sunarso, S. Baumann, J.M. Serra, W.A. Meulenberg, S. Liu, Y.S. Lin, and J.C. Diniz da Costa. Mixed ionic electronic conducting (MIEC) ceramic-based membranes for oxygen separation. *Journal of Membrane Science*, 320:13 – 41, 2008.

[5] H.J.M Bouwmeester, Kruidhof H., and A.J. Burggraaf. Importance of the surface exchange kinetics as rate limiting step in oxygen permeation through mixed-conduction oxides. *Solid State Ionics*, 72:185–194, 1994.

[6] J. Gurauskis, Ø.F. Lohne, and K. Wiik. $La_{0.2}Sr_{0.8}Fe_{0.8}Ta_{0.2}O_{3-\delta}$ based thin film membranes with surface modification for oxygen production. *Solid State Ionics*, 225(0):703 – 706, 2012.

[7] N. Wagner. Permeation and Stability Properties of Asymmetric and Disk Shaped Oxygen Permeable Membranes Intended for Syn-Gas Production. Diploma thesis, Norwegian University of Science and Technology, August 2012.

[8] V V Kharton, A A Yaremchenko, A V Kovalevsky, A P Viskup, E N Naumovich, and P F Kerko. Perovskite-type oxides for high-temperature oxygen separation membranes. *Journal of Membrane Science*, 163:307–317, 1999.

[9] S. P. S. Badwal and F. T. Ciacchi. Ceramic Membrane Technologies for Oxygen Separation. *Advanced Materials*, 13(12-13):993–996, July 2001.

[10] H.N.H. Bouwmeester and A. Burggraaf. *Dense Ceramic Membranes for Oxygen Separation, in Handbook of Solid State Electrochemistry.* CRC Press, 1997.

[11] V. M. Goldschmidt, T. F. W. Barth, G. Lunde, and W. Zachariasen. *Geochemische Verteilungsgesetze der Elemente : 7. Die Gesetze der Krystallochemie.* Skrifter/Videnskapsselskapet i Kristiania, Oslo, Norway, 1926.

[12] Geir Watterud. *Determination of oxygen transport coefficients in perovskites and perovskite related materials with mixed conductivity.* PhD thesis, NTNU, 2005.

[13] Fossdal, A. and Menon, M. and Wærnhus, I. and Wiik, K. and Einarsrud, M.-A. and Grande, T. Crystal Structure and Thermal Expansion of $La_{1-x}Sr_xFeO_{3-\delta}$ Materials. *Journal of the American Ceramic Society*, 87(10):1952–1958, 2004.

[14] A.A. Yaremchenko, V.V. Kharton, A.L. Shaula, M.V. Patrakeev, and F.M.B. Marques. Transport Properties and Thermal Expansion of Perovskite-like $La_{0.3}Sr_{0.7}Fe(Al,Cr)O_{3-\delta}$ Ceramics. *Journal of the European Ceramic Society*, 25(12):2603 – 2607, 2005.

[15] M Søregaard, P.V. Hendriksen, and M. Mogensen. Oxygen Nonstoichiometry and Transport Properties of Strontium Substituted Lanthanum Ferrite. *Journal of Solid State Chemistry*, 180(4):1489 – 1503, 2007.

[16] J.E. Elshof, H.J.M. Bouwmeester, and H. Verweij. Oxygen transport through $La_{1-x}Sr_xFeO_{3-\delta}$ membranes. I. Permeation in air/He gradients. *Solid State Ionics*, 81:97–109, 1995.

[17] A. Fossdal, M-A. Einarsrud, and T. Grande. Phase relations in the pseudo-ternary system $La_2O_3 - SrO - Fe_2O_3$. *Journal of the American Ceramic Society*, 88(7), 2005.

[18] V.V. Kharton, A.L. Shaula, F.M.M. Snijkers, J.F.C. Cooymans, J.J. Luyten, A.A. Yaremchenko, A.A. Valente, E.V. Tsipis, J.R. Frade, F.M.B. Marques, and J. Rocha. Processing, stability and oxygen permeability of $Sr(Fe,Al)O_3$-based ceramic membranes. *Journal of Membrane Science*, 252(1-2):215 – 225, 2005.

[19] F. Massazza. The System $SrO - Al_2O_3$. *Chim. Ind.(Milan)*, 41:108–115, 1959.

[20] P.J. Gellings and H.J.M. Bouwmeester, editors. *The CRC Handbook of Solid State Electrochemistry.* CRC-Press, 1997. ISBN 0849389569.

[21] M. Mosleh, M. Sogaard, and P.V. Hendriksen. Kinetics and Mechanisms of Oxygen Surface Exchange on $La_{0.6}Sr_{0.4}FeO_{3-\delta}$ Thin Films. *Journal of The Electrochemical Society*, 156(4):B441, 2009.

[22] D.S. Lagergren. Nanostructuring of Oxygen Permeable Membrane Surfaces by Wet Chemical Etching. Specialization project, Norwegian University of Science and Technology, December 2011.

[23] P. Wibe. Optimization of Strength and Permeability of Tape casted Porous $La_{0.2}Sr_{0.8}Fe_{0.8}Ta_{0.2}O_{3-\delta}$. Diploma thesis, Norwegian University of Science and Technology, July 2012.

[24] Uwe Beuscher and Charles H. Gooding. The permeation of binary gas mixtures through support structures of composite membranes. *Journal of Membrane Science*, 150(1):57 – 73, 1998.

[25] JW Veldsink, GF Versteeg, and WPM Van Swaaij. An experimental study of diffusion and convection of multicomponent gases through catalytic and non-catalytic membranes. *Journal of membrane science*, 92(3):275–291, 1994.

[26] R. Datta, S. Dechapanichkul, JS Kim, LY Fang, et al. A generalized model for the transport of gases in porous, non-porous, and leaky membranes. I. Application to single gases. *Journal of membrane science*, 75(3):245–263, 1992.

[27] H. Yasuda and JT Tsai. Pore size of microporous polymer membranes. *Journal of Applied Polymer Science*, 18(3):805–819, 1974.

[28] F.w. Altena, H.A.M. Knoef, H. Heskammp, D. Bargeman, and C.A. Smolders. Some Comments on the Applicability of Gas Permeation Methods to Characterize Porous Membranes Based on Improved Experimental Accuracy and Data Handling. *Journal of Membrane Science*, 12(3):313–322, 1982.

[29] A.S. Ziarani and R. Aguilera. Knudsen's Permeability Correction for Tight Porous Media. *Transport in porous media*, 91(1):239–260, 2012.

[30] H. Salmang and H. Scholze. *Keramik, 7., vollstandig neubearbeitete und erweiterte Auflag.* Springer Berlin Heidelberg New York, 2007. ISBN 3-540-63273-5.

[31] B.J. Berne and R. Pecora. *Dynamic Light Scattering: With Applications to Chemistry, Biology, and Physics.* Dover Publications, 1976.

[32] T. N. Phung. Theoretical density of LSFAl2882, PhD student at University Twente, email: t.phungnhuttan@tnw.utwente.nl.

[33] ICDD. ICDD PDF-4+ Database. `http://www.icdd.com/products/pdf4.htm`, December 2012.

[34] K. Kadoya, N. Matsunaga, and A. Nagashima. *Viscosity and thermal conductivity of dry air in the gaseous phase.* American Chemical Society and the American Institute of Physics for the National Bureau of Standards, 1985.

[35] R. D. Shannon. Revised effective ionic radii and systematic studies of interatomic distances in halides and chalcogenides. *Acta Crystallographica Section A*, 32(5):751–767, Sep 1976.

Appendix A

Calculation of the Goldschmidt Tolerance Factor

Calculation of the Goldschmidt tolerance factor for $La_{0.2}Sr_{0.8}Fe_{0.8}Al_{0.2}O_{3\text{-}\delta}$ was done using ionic radii reported by Shannon, R.D. [35]. The coordination number used for the A-site cations is 12, and the coordination number used for the B-site cations is 6. Fe^{3+} is considered to be high spin (HS) and the amount of Fe^{3+} and Fe^{4+} in the crystal lattice is determined by electron neutrality.

An assumption needed to calculate the Goldschmidt tolerance factor is that $\delta = 0$, and thus all the iron ions will be Fe^{4+}-ions. However this is not the case for LSFAl2882, therefore both extremes are calculated (all iron as either Fe^{4+} or Fe^{3+}). It is also assumed that the A and B radii can be approximated by the weighted radii of the different A and B-site cations.

Table A.1: *Cation radii, from [35]*

Element	**Coordination Number**	**Ionic radii**
La^{3+}	12	1.36
Sr^{2+}	12	1.44
Fe^{3+}(HS)	6	0.645
Fe^{4+}	6	0.585
Al^{3+}	6	0.535
O^{2-}	6	1.4

$$\tau_{G(Fe^{4+})} = \frac{((1.36 \cdot 0.2) + (1.44 \cdot 0.8)) + 1.4}{\sqrt{2}(((0.585 \cdot 0.8) + (0.535 \cdot 0.2)) + 1.4)} = 1.01 \qquad \text{(A.1)}$$

$$\tau_{G(Fe^{3+})} = \frac{((1.36 \cdot 0.2) + (1.44 \cdot 0.8)) + 1.4}{\sqrt{2}(((0.645 \cdot 0.8) + (0.535 \cdot 0.2)) + 1.4)} = 0.987 \tag{A.2}$$

To predict if LSFAl2882 is a more stable cubic perovskite than $La_{0.2}Sr_{0.8}FeO_{3\text{-}\delta}$ (LSF) the Goldschmidt tolerance factor is also calculated for LSF:

$$\tau_{G_{LSF}(Fe^{4+})} = \frac{((1.36 \cdot 0.2) + (1.44 \cdot 0.8)) + 1.4}{\sqrt{2}(0.585 + 1.4)} = 1.01 \tag{A.3}$$

$$\tau_{G_{LSF}(Fe^{3+})} = \frac{((1.36 \cdot 0.2) + (1.44 \cdot 0.8)) + 1.4}{\sqrt{2}(0.645 + 1.4)} = 0.976 \tag{A.4}$$

Appendix B

Tables of Batch compositions

During the work leading up to this thesis different compositions of LSFAl was prepared, where the aim was to try and produce a single phase powder. In the tables below the amount of different starting compounds, and the relative deviation from ideal stoichiometry can be seen. Batch #5 and #6 were used to prepare the porous supports made in this work.

Table B.1: *LSFAl 2882, Batch 1*

Chemical	**Amount s[g]**	**Moles**	**Deviation of ratio X_1 to X_2**
La_2O_3	14.385	0.088303	-0.088%
$SrCO_3$	52.095	0.35290	+0.088%
Fe_2O_3	28.205	0.35325	-0.094%
Al_2O_3	4.498	0.08829	+0.094%

Table B.2: *LSFAl 2882, Batch 2*

Chemical	**Amount s[g]**	**Moles**	**Deviation of ratio X_1 to X_2**
La_2O_3	2.0003	0.012279	-0.008%
$SrCO_3$	7.2498	0.049112	+0.008%
Fe_2O_3	3.9216	0.049116	-0.046%
Al_2O_3	0.6257	0.012273	+0.046%

Table B.3: *LSFAl 2882, Batch 3*

Chemical	**Amount s[g]**	**Moles**	**Deviation of ratio X_1 to X_2**
La_2O_3	14.006	0.085977	-0.026%
$SrCO_3$	50.7536	0.34382	+0.026%
Fe_2O_3	27.445	0.34373	+0.018%
Al_2O_3	4.3817	0.085948	-0.018%

Table B.4: *LSFAl 2882, Batch 4*

Chemical	**Amount s[g]**	**Moles**	**Deviation of ratio X_1 to X_2**
La_2O_3	20.0075	0.122817	-0.025%
$SrCO_3$	72.502	0.49115	+0.025%
Fe_2O_3	39.2158	0.491153	+0.027%
Al_2O_3	6.2615	0.12282	-0.027%

Table B.5: *LSFAl 4682, Batch 1*

Chemical	**Amount s[g]**	**Moles**	**Deviation of ratio X_1 to X_2**
La_2O_3	4.0006	0.024558	-0.07%
$SrCO_3$	5.4374	0.036834	+0.07%
Fe_2O_3	3.9209	0.049107	+0.084%
Al_2O_3	0.6264	0.012287	-0.084%

Table B.6: *LSFAl 20808515, Batch 1*

Chemical	**Amount s[g]**	**Moles**	**Deviation of ratio X_1 to X_2**
La_2O_3	2.0009	0.012283	-0.031%
$SrCO_3$	7.2503	0.049115	+0.031%
Fe_2O_3	4.1668	0.052187	-0.214%
Al_2O_3	0.4685	0.00091898	+0.214%

Table B.7: *LSFAl 2882 with nano-sized alumina, Batch 1*

Chemical	**Amount s[g]**	**Moles**	**Deviation of ratio X_1 to X_2**
La_2O_3	4.0039	0.024578	-0.077%
$SrCO_3$	14.5016	0.098237	+0.077%
Fe_2O_3	7.8460	0.098266	-0.034%
Al_2O_3	1.2520	0.024558	+0.034%

Appendix C

Calculation of the amount of different precursors needed to make LSFAl

The calculation of the amount of each precursor needed to produce $La_{0.2}Sr_{0.8}Fe_{0.8}Al_{0.2}O_{3\text{-}\delta}$ is given below. Note that the amount of oxygen needed to complete the reaction is irrelevant, as it is not the limiting reactant.

The number of moles of a substance, x, is given by:

$$n_x = \frac{m_x}{M_x}$$

Where m_x is the amount of x and M_x is the molar mass of x. The following relations are observed for the composition described above (LSFA12882):

$$n_{La} = n_{Al} = n_a$$

$$n_{Sr} = n_{Fe} = n_b$$

Furthermore the following relationship between n_a and n_b holds:

$$n_b = 4{\cdot}n_a$$

If the amount of one precursor is chosen to be x, then the amount of the remaining precursors needed to make LSFAl2882 can be calculated. An example is given below for choosing La_2O_3 as the starting precursor.

$$m_{La_2O_3} = x \rightarrow n_{La_2O_3} = \frac{x}{M_{La_2O_3}} = \frac{1}{2}n_{La} \tag{C.1}$$

$$n_{La} = 2{\cdot}n_{La_2O_3} = \frac{2x}{M_{La_2O_3}} \tag{C.2}$$

$$n_{SrCO_3} = n_{Sr} = 4 \cdot n_{La} \rightarrow m_{SrCO_3} = \frac{8x}{M_{La_2O_3}} \cdot M_{SrCO_3} \tag{C.3}$$

$$n_{Fe_2O_3} = \frac{1}{2} n_{Fe} = \frac{1}{2} 4 \cdot n_{La} \rightarrow m_{Fe_2O_3} = \frac{4x}{M_{La_2O_3}} \cdot M_{Fe_2O_3} \tag{C.4}$$

$$n_{Al_2O_3} = \frac{1}{2} n_{Al} = \frac{1}{2} \cdot n_{La} \rightarrow m_{Al_2O_3} = \frac{x}{M_{La_2O_3}} \cdot M_{Al_2O_3} \tag{C.5}$$

Here x is the amount of La_2O_3 (in grams) in the raw powder mixture before calcination, which should yield $La_{0.2}Sr_{0.8}Fe_{0.8}Al_{0.2}O_{3\text{-}\delta}$ after calcination.

Appendix D

Calculations of True Porosity

The true porosity of a sample can be calculated using the ISO standard: *ISO-5017:1998 - Determination of bulk density, apparent porosity, and true porosity.* The sample was first weighed (m_1) and then put under vacuum for 30 minutes. The sample was then submerged in isopropanol (still under vacuum) for 30 minutes. Finally the vacuum was released and the sample rested (still submerged) for 30 minutes under atmospheric pressure before weighed still submerged (m_2), and finally weighed unsubmerged (m_3). Table D.1 shows the recorded weight measurements for two samples, and the true porosity was calculated according to Equation D.1.

Table D.1: *True porosity of porous supports*

Sample	m_1	m_2	m_3	π_t
# 1	0.1032	0.0881	0.1256	61.2%
# 2	0.0972	0.0830	0.1185	61.4%
Average	-	-	-	61.3%

$$\rho_b = \frac{m_1}{m_3 - m_2} \cdot \rho_{liq}$$

$$\pi_t = \frac{\rho_t - \rho_b}{\rho_t} \cdot 100\% \tag{D.1}$$

Appendix E

Surface Area Weighted Mean

When calculating an average from values with uncertainty the best practice is to use a weighted mean. The equations for calculating the weighted mean and the weighted uncertainty is given under.

$$\overline{x} = \frac{\sum_i \frac{x_i}{\sigma_i^2}}{\sum_i \frac{1}{\sigma_i^2}} \tag{E.1}$$

$$\sigma_{\overline{x}} = \frac{1}{\sqrt{\sum_i \frac{1}{\sigma_i^2}}} \tag{E.2}$$

For the data given in Table 4.2 the calculated weighted mean and uncertainty is:

$$\overline{x} = \frac{(\frac{0.9744}{0.0025^2} + \frac{0.9704}{0.0006^2})}{(\frac{1}{0.0025^2} + \frac{1}{0.0006^2})} = 0.9706 \tag{E.3}$$

$$\sigma_{\overline{x}} = \frac{1}{\sqrt{(\frac{1}{0.0025^2} + \frac{1}{0.0006^2})}} = 0.0006 \tag{E.4}$$

Appendix F

BET Measurement Data

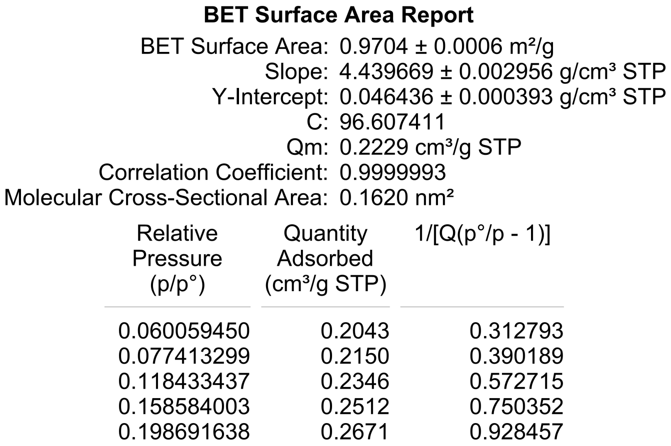

BET Surface Area Report

BET Surface Area: 0.9704 ± 0.0006 m²/g
Slope: 4.439669 ± 0.002956 g/cm³ STP
Y-Intercept: 0.046436 ± 0.000393 g/cm³ STP
C: 96.607411
Qm: 0.2229 cm³/g STP
Correlation Coefficient: 0.9999993
Molecular Cross-Sectional Area: 0.1620 nm²

Relative Pressure (p/p°)	Quantity Adsorbed (cm³/g STP)	1/[Q(p°/p - 1)]
0.060059450	0.2043	0.312793
0.077413299	0.2150	0.390189
0.118433437	0.2346	0.572715
0.158584003	0.2512	0.750352
0.198691638	0.2671	0.928457

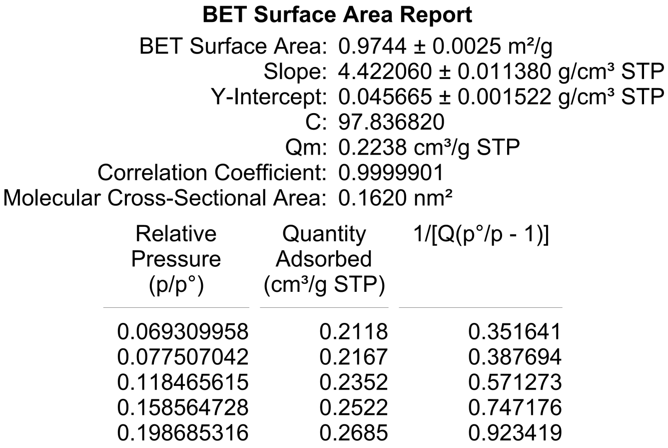

BET Surface Area Report

BET Surface Area: 0.9744 ± 0.0025 m²/g
Slope: 4.422060 ± 0.011380 g/cm³ STP
Y-Intercept: 0.045665 ± 0.001522 g/cm³ STP
C: 97.836820
Qm: 0.2238 cm³/g STP
Correlation Coefficient: 0.9999901
Molecular Cross-Sectional Area: 0.1620 nm²

Relative Pressure (p/p°)	Quantity Adsorbed (cm³/g STP)	1/[Q(p°/p - 1)]
0.069309958	0.2118	0.351641
0.077507042	0.2167	0.387694
0.118465615	0.2352	0.571273
0.158564728	0.2522	0.747176
0.198685316	0.2685	0.923419

Figure F.1: *BET measurement data*

Appendix G

EDS of Asymmetric Membrane

The EDS analysis of the primary and secondary phases seen from SEM analysis can be seen in Figure G.1

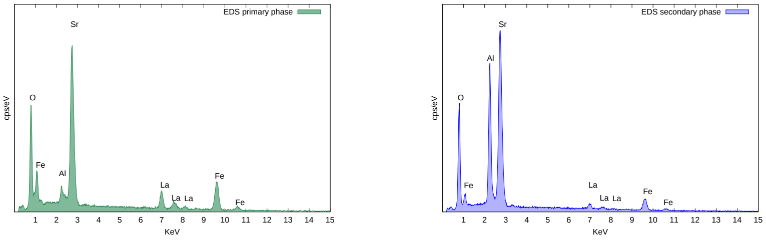

(a) EDS primary phase **(b)** EDS secondary phase

Figure G.1: *EDS analysis of the two seen phases from SEM micrograph*

The overlap of the two EDS-spectra can be seen in Figure G.2

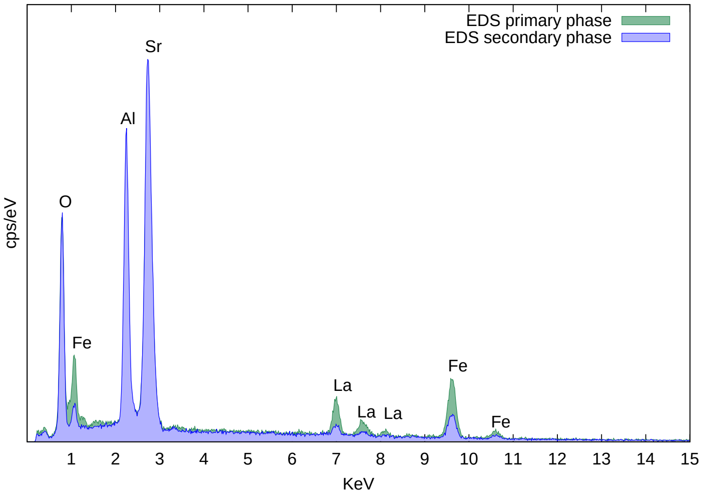

Figure G.2: *EDS analysis of the dense layer of the asymmetric membrane*

Appendix H

Topas analysis - amount of the Secondary Phase

The relative amount of the secondary $SrAl_2O_4$ phase was investigated using the software Topas and the results can be seen in Figure H.1. The relative amount was calculated using the cubic perovskite structure for LSF28 ($La_{0.2}Sr_{0.8}FeO_{3\text{-}\delta}$). In addition the patterns were matched by using the rombohedral perovskite structure for LSF26 ($La_{0.4}Sr_{0.6}FeO_{3\text{-}\delta}$), and as seen from the figure the rombohedral analysis seems to fit better than the cubic both for the porous support pattern and the pattern for LSFAl2882 powder prepared with nano-alumina.

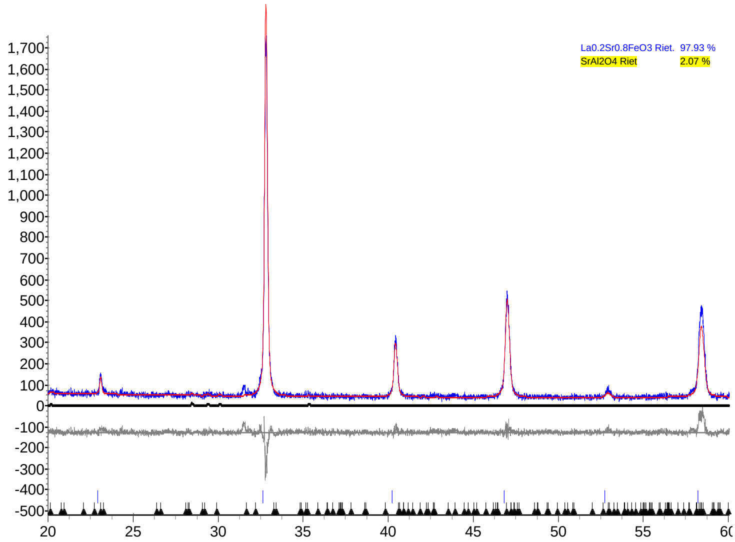

(a) Topas analysis of the coars LSFAl2882 powder

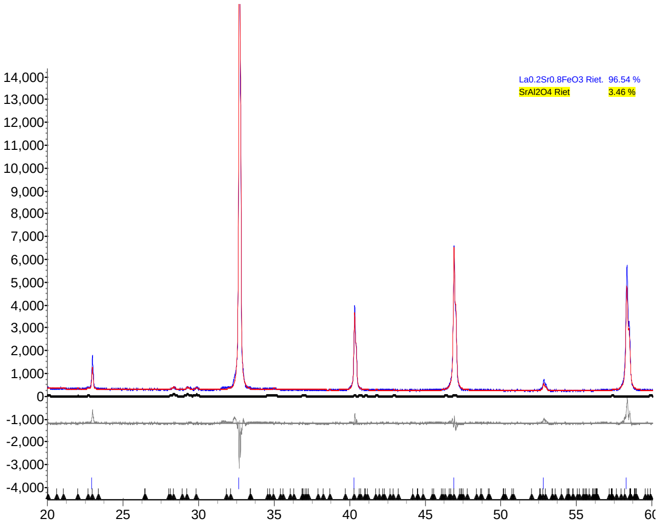

(b) Topas analysis of the porous support (matched with cubic LSF)

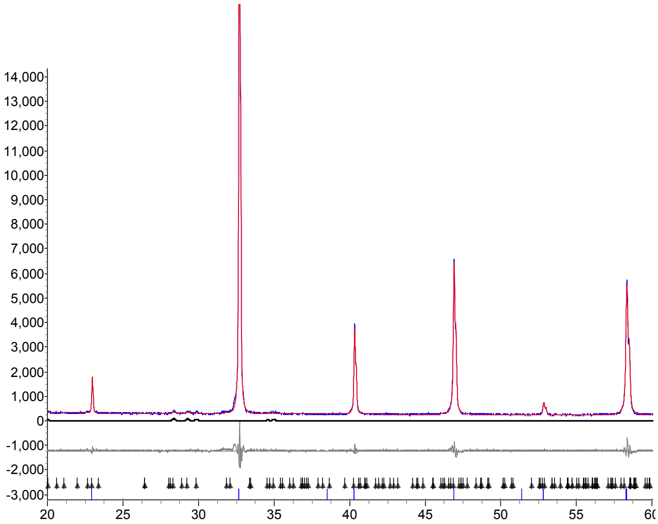

(c) Topas analysis of the porous support (matched with rombohedral LSF)

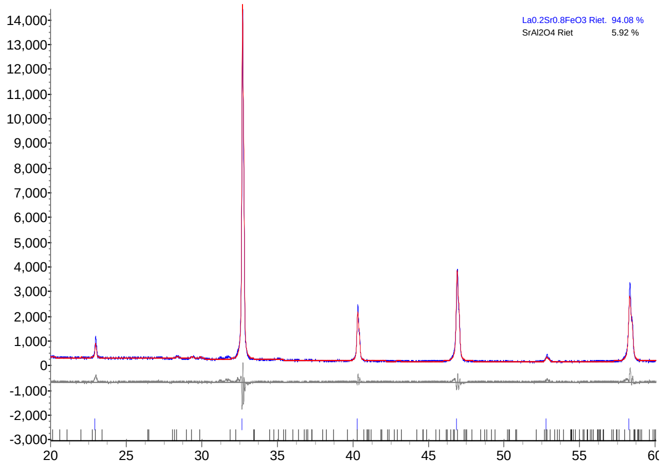

(d) Topas analysis of the asymmetric membrane (matched with cubic LSF)

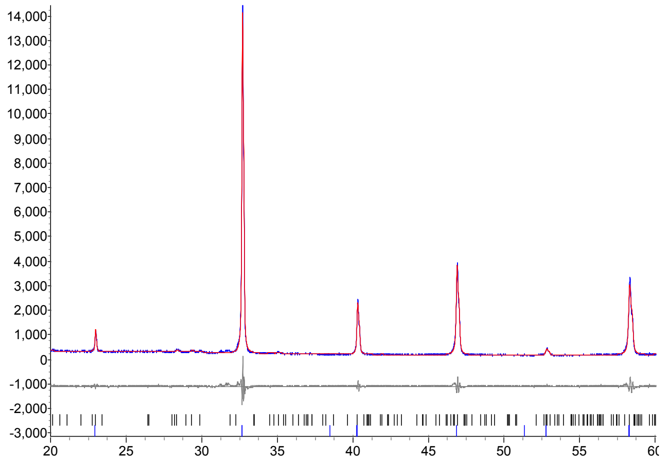

(e) Topas analysis of the asymmetric membrane (matched with rombohedral LSF)

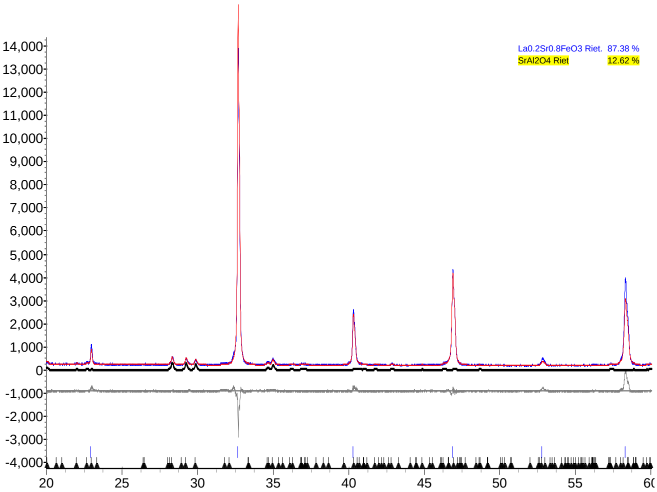

(f) Topas analysis of the LSFAL powder prepared with nano-alumina (matched with cubic LSF)

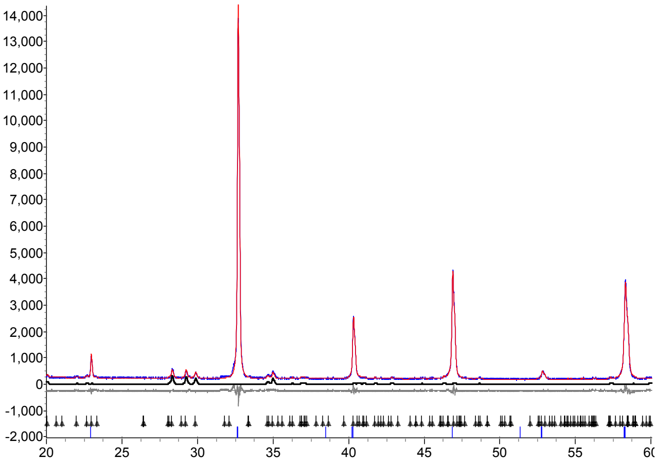

(g) Topas analysis of the LSFAL powder prepared with nano-alumina (matched with rombohedral LSF)

Figure H.1: *Phase analysis by Topas*